Quasi-static cyclic in-plane tests on masonry components 2016/2017

Esposito, Rita; Ravenshorst, Geert

Publication date
2017

Document Version
Final published version

Citation (APA)
Esposito, R., & Ravenshorst, G. (2017). *Quasi-static cyclic in-plane tests on masonry components 2016/2017*. Delft University of Technology.

Project number	C31B67
File reference	C31B67WP3-4
Date	10 August 2017
Corresponding author	Rita Esposito (r.esposito@tudelft.nl)

TU Delft Large-scale testing campaign 2016

QUASI-STATIC CYCLIC IN-PLANE TESTS ON MASONRY COMPONENTS 2016/2017

Authors: Rita Esposito, Geert J.P. Ravenshorst
Collaborators: Edwin Meulman, Marina Damiola, Alessandro Pagani

***Cite as**: Esposito, R., and Ravenshorst, G.J.P. Quasi-static cyclic in-plane tests on masonry components 2016/2017. Report No. C31B67WP3-4, 10 August 2017. Delft University of Technology.*

This research work was funded by NAM Structural Upgrading stream.

Table of Contents

1 Introduction

Quasi-static cyclic tests on masonry components, such as walls, can capture the behaviour of vulnerable elements and thus serve as benchmarks for the validation of analysis methods. They allow studying the response of the element in terms of load and deformation capacity, failure mechanism and hysteresis behaviour. In-plane and out-of-plane tests are generally performed in this category.

Considering their importance, these tests have been included in the large-scale testing campaign to be performed at Delft University of Technology in 2016 within the NAM Structural Upgrading project. The campaign includes a total of six work packages (WPs), which focus on the characterisation of vulnerable elements for both the detached and terraced house typology. In particular, for the detached house typology the behaviour of flexible diaphragms and theirs connection with solid clay brick masonry walls is of interest, while for the terraced house typology, the behaviour of buildings made of calcium silicate element masonry is of interest. These two topics are developed, respectively, in WP4 and WP5 with respect to the characterisation at connection, sub-assemblage and assemblage level. In WP3, which is here discussed, only the behaviour of URM masonry walls is studied; however choices related to geometry, materials and boundary conditions of the component tests are directly related to the other two WPs ([1], [2]).

In this report the tests results related to the quasi-static cyclic in-plane tests on large-scale walls are presented. Section 2 shows the nomenclature adopted in this report. Section 3 reports a description of the in-plane tests performed in WP3. Section 4 gives an overview of the material properties determined via companion destructive tests. Section 5 presents the testing procedure for the in-plane shear-compression tests on large-scale walls. Section 6 shows the experimental results in terms of hysteresis behaviour, force and displacement capacity, crack pattern evolution and dissipated energy. Section 7 reports an overview of the results and compares the performances of the various walls adopting the bilinear curve. In Section 8 the force and displacement capacity of each wall is evaluated by adopting the analytical formulation proposed by Eurocode 8 [3] and NPR 9998:2017 [4] for the assessment of existing masonry structures; a comparison with experimental results is presented. Eventually, summary and conclusions are reported in Section 9.

2 Nomenclature

2.1 Symbols

α	Constant adopted in the NPR 9998 [4]
β	Constant adopted in the NPR 9998 [4]
μ	Masonry (bed joint) shear strength coefficient
μ_b	Ductility factor determined by the bilinear approximation
μ_{res}	Masonry (bed joint) residual shear strength coefficient
ε_p	Strain associated with peak strength in vertical compression test
$\varepsilon_{p,h}$	Strain associated with peak strength in horizontal compression test
σ_v	Overburden stress applied at the top of the wall during the in-plane test
d_1	Horizontal distance between the vertical actuators in the in-plane set-up
d_2	Reduced level arm for the vertical forces in the case of in-plane tests on squat walls.
d_r^-	(Experimental) maximum drift in the negative loading direction
d_r^+	(Experimental) maximum drift in the positive loading direction
d_{r-b}	Ultimate drift for the bilinear approximation
d_{r-dt}	Ultimate drift for walls subject to diagonal tension failure in agreement with NPR 9998 [4]
d_{r-f}	Ultimate drift for walls subject to flexural failure in agreement with Eurocode 8 [3]
d_{r-r}	Ultimate drift for walls subject to rocking failure in agreement with NPR 9998 [4]
d_{r-s}	Ultimate drift for walls subject to bed joint sliding failure in agreement with NPR 9998 [4]
d_{r-sh}	Ultimate drift for walls subject to shear failure in agreement with Eurocode 8 [3]
d_{r-tc}	Ultimate drift for walls subject to toe crushing failure in agreement with NPR 9998 [4]
f_b	Normalised compressive strength of masonry unit
f_{bt}	Flexural strength of masonry unit
f_m	Compressive strength of masonry mortar
f_{mt}	Flexural strength of masonry mortar
$f_m^{'}$	Compressive strength of masonry in the direction perpendicular to the bed joints
$f_{m,h}^{'}$	Compressive strength of masonry in the direction parallel to the bed joints
f_{x1}	Masonry flexural strength with the moment vector parallel to the bed joints and in the plane of the wall, which generates a plane of failure parallel to the bed joints
f_{x2}	Masonry flexural strength with the moment vector orthogonal to the bed joints and in the plane of the wall, which generates a plane of failure perpendicular to the bed joints
f_{x3}	Masonry flexural strength with the moment vector orthogonal to the plane of the wall
f_{v0}	Masonry (bed joint) initial shear strength
$f_{v0,res}$	Masonry (bed joint) residual initial shear strength

f_w	Masonry uniaxial bond strength between the masonry unit and the mortar
l_j	Length of the mortar bed joint in a masonry specimens
l_u	Length of the masonry unit as used in the construction of masonry
h_u	Height of the masonry unit as used in the construction
t_j	Thickness of bed and head joints
t_u	Thickness of the masonry unit as used in the construction of masonry
t_w	Thickness of the wall
u	Horizontal displacement
u_{el}	Elastic horizontal displacement in the bilinear curve
u_u	Ultimate horizontal displacement in the bilinear curve
v_L	Vertical displacement in the left actuators
v_R	Vertical displacement in the right actuators
E_1	Secant elastic modulus of masonry subject to a compressive loading perpendicular to the bed joints, evaluated at 1/3 of the maximum stress
E_2	Secant elastic modulus of masonry subject to a compressive loading perpendicular to the bed joints, evaluated at 1/10 of the maximum stress
E_3	Chord elastic modulus of masonry subject to a compressive loading perpendicular to the bed joints, evaluated at between 1/10 and 1/3 of the maximum stress
$E_{1,h}$	Secant elastic modulus of masonry subject to a compressive loading parallel to the bed joints, evaluated at 1/3 of the maximum stress
$E_{2,h}$	Secant elastic modulus of masonry subject to a compressive loading parallel to the bed joints, evaluated at 1/10 of the maximum stress
$E_{3,h}$	Chord elastic modulus of masonry subject to a compressive loading parallel to the bed joints, evaluated at between 1/10 and 1/3 of the maximum stress
F_i	Vertical force applied at the *i-th* vertical actuator (with i = 1, 2, 3, 4)
F_L	Vertical force applied on the actuators on the front-left side of the specimens during the in-plane test.
F_R	Vertical force applied on the actuators on the front-right side of the specimens during the in-plane test.
G	Self-weight of the masonry
G_{f-c}	Fracture energy in compression for loading perpendicular to the bed joints
$G_{f-c,h}$	Fracture energy in compression for loading parallel to the bed joints
H_a	Distance between the top side of the wall and the point of application of the horizontal force
H_w	Height of the wall
K	Initial stiffness of the wall
K_{el}	Stiffness of the bilinear curve
L_w	Length of the wall
P	Pre-compression load $P = \sigma_v / \left(L_w t_w \right)$
V^-	Maximum base shear force in the negative loading direction
V^+	Maximum base shear force in the positive loading direction
V_f	Analytical estimation of the maximum base shear force of a wall subject to flexural failure in agreement with Eurocode 8 [3].

V_{dt}	Analytical estimation of the maximum base shear force of a wall subject to diagonal tension failure in agreement with NPR 9998 [4]
V_{tc}	Analytical estimation of the maximum base shear force of a wall subject to toe crushing failure in agreement with NPR 9998 [4]
V_r	Analytical estimation of the maximum base shear force of a wall subject to rocking failure in agreement with NPR 9998 [4]
V_s	Analytical estimation of the maximum base shear force of a wall subject to bed joint sliding failure in agreement with NPR 9998 [4]
V_{sh}	Analytical estimation of the maximum base shear force of a wall subject to shear failure in agreement with Eurocode 8 [3].
V_u	Maximum base shear force in the bilinear curve
W_t	Weight of the top steel system

2.2 Abbreviations

Avg.	Average
C.o.V.	Coefficient of variation
CS	Calcium silicate
St. dev.	Standard deviation

3 Description of the specimens

Six masonry walls were tested under cyclic in-plane tests. Table 1 lists the various tests reporting geometry, overburden value, boundary conditions and date of testing. Figure 1 shows an overview of the walls before the test.

During the experimental campaign 2015 [5], six tests were performed, but a limited drift of the wall could be achieved due to limitation of the set-up. On the basis of the lessons learned, the set-up was modified [2] and a repetition of a wall made of calcium silicate brick (TUD_COMP-20) was performed.
Three walls made of solid clay brick masonry were tested having dimensions 3x2.7 m. One single wythe wall was tested under double clamped configuration in order to observe a diagonal shear failure mode (TUD_COMP-21). Two double-wythe walls (steensmuren) were tested in cantilever configuration (TUD_COMP-22 and TUD_COMP-23). The specimen TUD_COMP-23 includes an asymmetric opening (see Appendix A), to investigate the formation of diagonal cracks. The dimensions of this walls and of the opening have been defined in agreement with the dimension used in the testing campaign 2016 performed by EUCentre [6], which are representative of the building stock. The test does not investigate the spandrel effect.
Two walls made of calcium silicate element masonry with dimensions of approximatively 1.3x2.7 m were tested. Specimen TUD_COMP-24 was tested in double clamped configuration, while specimen TUD_COMP-25 was tested in cantilever configuration. The aim of these tests is twofold: 1) to compare the in-plane behaviour of walls made of calcium silicate element masonry with the one made of calcium silicate bricks that were tested in 2015; 2) as a support for the pushover cyclic test perform on a two-story high building made of calcium silicate element (WP5).

Table 1 – Quasi-static cyclic in-plane tests performed in WP3.

Sample name	Testing date	Unit type	L_w	H_w	t_w	σ_v	Boundary conditions
			mm	mm	mm	MPa	
TUD_COMP-20	8/12/16	CS brick	1110	2778	102	0.63	Cantilever
TUD_COMP-21	4/4/17	Solid clay brick	3070	2710	100	0.36	Fix-Fix
TUD_COMP-22	11/4/17	Solid clay brick	2960	2710	210	0.36	Cantilever
TUD_COMP-23 (with opening)	26/4/17	Solid clay brick	3070	2710	210	0.36	Cantilever
TUD_COMP-24	22/12/16	CS elements	977	2743	100	0.6	Fix-Fix
TUD_COMP-25	16/12/16	CS elements	977	2743	100	0.6	Cantilever

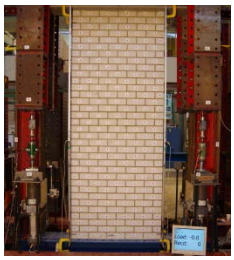
(a) TUD_COMP-20

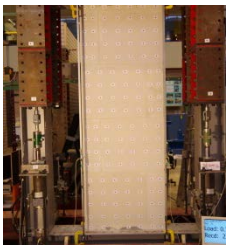
(b) TUD_COMP-24

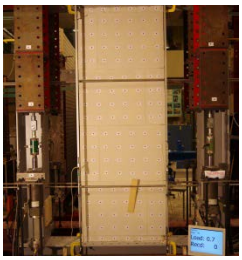
(c) TUD_COMP-25

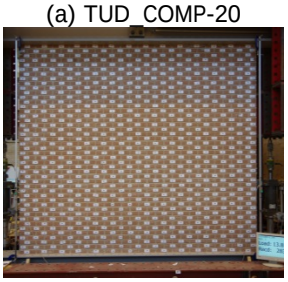
(d) TUD_COMP-21

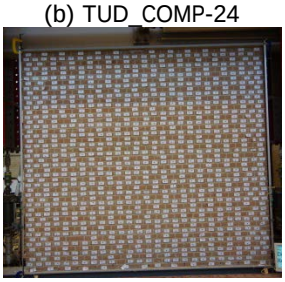
(e) TUD_COMP-22

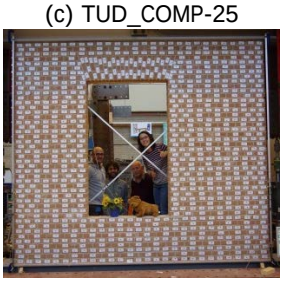
(f) TUD_COMP-23

Figure 1 – Overview of quasi-static cyclic in-plane tests performed in WP3.

4 Material properties

The characterisation of every masonry type has been carried out by performing destructive laboratory tests on both masonry and its constituents. The aim of these tests is twofold: 1) to serve as companion tests for the large-scale tests on components (WP3) and assemblage (WP5), 2) to study the correlation between various material testing methods (WP1).

In this study three masonry types have been studied: (1) calcium silicate (CS) brick masonry, (2) clay brick masonry and (3) calcium silicate (CS) element masonry. The first two types are made in small masonry units (brick) and general purpose mortar. The last type is made of large masonry units (elements) and thin mortar layer. In Table 2 the dimensions of the masonry units (length l_u, height h_u and thickness t_u) and the average thickness of mortar joint t_j are listed.
In Table 3, Table 4, Table 5 and Table 6 the material properties of CS brick, single wythe clay brick, double wythe clay brick and CS element masonry are reported. Detailed information on the tests can be found in the dedicated reports in Refs. [7], [8] and [9]. Please note that test on CS brick masonry were previously performed in 2015, consequently in this testing campaign only vertical compression, shear and bond wrench test were performed For a complete overview of all properties please see Refs. [7].

Table 2 – Dimensions of masonry units and mortar joint.

Masonry type	Unit			Bed joint	Head joint
	l_u	h_u	t_u	t_j	t_j
	mm	mm	mm	mm	mm
CS brick	210	71	100	10	10
Solid clay	210	50	100	10	10
CS element	897	643	100	3	2

Table 3 – Material properties of CS brick masonry built in August 2016 (extracted from [7]).

Property		Symbol	Unit	Average	St. dev.	C.o.V.	No. tests
Compressive strength of mortar		f_m	MPa	**7.57**	0.46	0.06	150
Flexural strength of mortar		f_{mt}	MPa	**3.21**	0.18	0.05	75
Normalised compressive strength of masonry unit		f_b	MPa	**13.26**	1.71	0.13	6
Compressive strength of masonry in the direction perpendicular to bed joints		f'_m	MPa	**6.35**	0.32	0.05	
Density of masonry		ρ	Kg/m^3	**1805**			
Elastic modulus of masonry in the direction perpendicular to bed joints evaluated at	1/3 of the maximum stress	E_1	MPa	**4972**	568	6	
	1/10 of the maximum stress	E_2	MPa	**8206**	1008	6	
	between 1/10 and 1/3 of the maximum stress	E_3	MPa	**4265**	527	6	
Poisson ratio of masonry in the direction perpendicular to bed joints		ν		**0.16**	0.03	0.19	
Fracture energy in compression for loading perpendicular to bed joints*		$G_{f\text{-}c}$	N/mm	**20.0**	3.43	0.17	
Flexural bond strength		f_w	MPa	**0.12**	0.01	0.12	7
Masonry (bed joint) initial shear strength		f_{v0}	MPa	**0.13**	-	-	9
Masonry (bed joint) shear friction coefficient		μ		**0.50**	-	-	
Residual masonry (bed joint) shear strength		$f_{v0,res}$	MPa	**0.01**	-	-	
Residual masonry (bed joint) shear friction coefficient		μ_{res}		**0.52**	-	-	

Table 4 – Material properties of single wythe clay brick masonry built in August 2016 (extracted from [8]).

Property	Symbol	Unit	Single wythe clay brick			
			Average	St. dev.	C.o.V.	Number of test
Compressive strength of mortar	f_m	MPa	**3.81**	0.34	0.09	108
Flexural strength of mortar	f_{mt}	MPa	**1.40**	0.17	0.12	54
Normalised compressive strength of masonry unit	f_b	MPa	**28.31**	2.92	0.10	9
Flexural strength of masonry unit	f_{bt}	MPa	**6.31**	0.72	0.11	8
Elastic modulus of masonry unit	E_b	MPa	**6196**			
Density of masonry	ρ	Kg/m^3	**1708**	71	0.04	19
Compressive strength of masonry in the direction perpendicular to bed joints	f'_m	MPa	**14.02**	0.56	0.04	6
Elastic modulus of masonry in the direction perpendicular to bed joints	E_1	MPa	**4380**	605	0.14	6
	E_2	MPa	**4068**	783	0.19	
	E_3	MPa	**4590**	603	0.13	
Fracture energy in compression for loading perpendicular to bed joints	$G_{f\text{-}c}$	N/mm	**28.52**	3.40	0.12	
Poisson ratio of masonry in the direction perpendicular to bed joints	ν		**0.14**	0.02	0.11	
Strain corresponding to peak strength in compression in the direction perpendicular to bed joints	ε_p	‰	**4.3**	0.40	0.10	
Compressive strength of masonry in the direction parallel to bed joints	$f'_{m,h}$	MPa	**13.11**	2.41	0.18	6
Elastic modulus of masonry in the direction parallel to bed joints	$E_{1,h}$	MPa	**3332**	565	0.17	6
	$E_{2,h}$	MPa	**3664**	689	0.19	
	$E_{3,h}$	MPa	**3207**	592	0.18	
Fracture energy in compression for loading parallel to bed joints	$G_{f\text{-}c,h}$	N/mm	**35.1**	6.63	0.19	
Strain corresponding to peak strength in compression in the direction parallel to bed joints	$\varepsilon_{p,h}$	‰	**5.8**	1.0	0.19	
Masonry flexural strength with the moment vector parallel to the bed joints and in the plane of the wall	f_{x1}	MPa	**0.16**	0.03	0.18	5
Masonry flexural strength with the moment vector orthogonal to the bed joint and in the plane of the wall	f_{x2}	MPa	**0.65**	0.17	0.25	5
Masonry flexural strength with the moment vector orthogonal to the plane of the wall	f_{x3}	MPa	**0.46**	0.09	0.20	7
Flexural bond strength	f_w	MPa	**0.15**	0.05	0.32	15
Masonry (bed joint) initial shear strength	f_{v0}	MPa	**0.20**	**-**	-	7
Masonry (bed joint) shear friction coefficient	μ	-	**0.69**	**-**	-	
Residual masonry (bed joint) initial shear strength	$f_{v0,res}$	MPa	**0.05**	**-**	-	8
Residual masonry (bed joint) shear friction coefficient	μ_{res}	-	**0.60**	**-**	-	

Table 5 – Material properties of double wythe clay brick masonry built in August 2016 (extracted from [8]).

Property	Symbol	Unit	Double wythe clay brick			
			Average	St. dev.	C.o.V.	Number of test
Compressive strength of mortar	f_m	MPa	See Table 4			
Flexural strength of mortar	f_{mt}	MPa				
Normalised compressive strength of masonry unit	f_b	MPa				
Flexural strength of masonry unit	f_{bt}	MPa				
Elastic modulus of masonry unit	E_b	MPa				
Density of masonry	ρ	Kg/m^3				
Compressive strength of masonry in the direction perpendicular to bed joints	f'_m	MPa	**9.24**	1.19	0.13	12
Elastic modulus of masonry in the direction perpendicular to bed joints	E_1	MPa	**2771**	475	0.17	
	E_2	MPa	**2646**	929	0.35	
	E_3	MPa	**2951**	413	0.14	
Fracture energy in compression for loading perpendicular to bed joints	$G_{f\text{-}c}$	N/mm	**34.8**	7.7	0.22	
Poisson ratio of masonry in the direction perpendicular to bed joints	ν		**0.12**	0.02	0.20	
Strain corresponding to peak strength in compression in the direction perpendicular to bed joints	ε_p	‰	**4.06**	0.70	0.17	
Compressive strength of masonry in the direction parallel to bed joints	$f'_{m,h}$	MPa	**9.15**	0.91	0.10	6
Elastic modulus of masonry in the direction parallel to bed joints	$E_{1,h}$	MPa	**4012**	676	0.17	
	$E_{2,h}$	MPa	**3954**	516	0.13	
	$E_{3,h}$	MPa	**4319**	1571	0.36	
Fracture energy in compression for loading parallel to bed joints	$G_{f\text{-}c,h}$	N/mm	**28.3**	4.3	0.15	
Strain corresponding to peak strength in compression in the direction parallel to bed joints	$\varepsilon_{p,h}$	‰	**4.6**	0.9	0.21	
Masonry flexural strength with the moment vector parallel to the bed joints and in the plane of the wall	f_{x1}	MPa	**0.14**	0.040	0.28	5
Masonry flexural strength with the moment vector orthogonal to the bed joint and in the plane of the wall	f_{x2}	MPa	**0.41**	0.06	0.14	5
Masonry flexural strength with the moment vector orthogonal to the plane of the wall	f_{x3}	MPa	**0.42**	0.02	0.05	5
Flexural bond strength	f_w	MPa	See Table 4			
Masonry (bed joint) initial shear strength	f_{v0}	MPa				
Masonry (bed joint) shear friction coefficient	μ	-				
Residual masonry (bed joint) initial shear strength	$f_{v0,res}$	MPa				
Residual masonry (bed joint) shear friction coefficient	μ_{res}	-				

Table 6 – Material properties of CS element masonry built in August 2016 (extracted from [9]).

Property	Symbol	Unit	Calcium silicate element			
			Average	St. dev.	C.o.V.	No. test
Compressive strength of mortar	f_m	MPa	**16.1**	1.48	0.09	36
Flexural strength of mortar	f_{mt}	MPa	**4.7**	1.04	0.22	18
Normalised compressive strength of masonry unit	f_b	MPa	**19.4**	2.69	0.14	25
Flexural strength of masonry unit	f_{bt}	MPa	**3.65**	0.21	0.06	18
Elastic modulus of masonry unit in compression	E_b	MPa	**8916**	7624	0.11	6
Density of masonry	ρ	Kg/m^3	**1824**	38	0.02	22
Compressive strength of masonry in the direction perpendicular to bed joints	f'_m	MPa	**13.93**	1.03	0.07	6
Elastic modulus of masonry in the direction perpendicular to bed joints	E_1	MPa	**8557**	1619	0.19	
	E_2	MPa	**9256**	2660	0.29	
	E_3	MPa	**8313**	1251	0.15	
Fracture energy in compression for loading perpendicular to bed joints	$G_{f\text{-}c}$	N/mm	**20.9**	5.47	0.26	
Poisson ratio of masonry in the direction perpendicular to bed joints	ν		**0.21**	0.40	0.20	
Strain corresponding to peak strength in compression in the direction perpendicular to bed joints	ε_p	‰	**2.01**	0.37	0.19	
Compressive strength of masonry in the direction parallel to bed joints	$f'_{m,h}$	MPa	**9.42**	1.63	0.17	6
Elastic modulus of masonry in the direction parallel to bed joints	$E_{1,h}$	MPa	**8416**	1445	0.17	
	$E_{2,h}$	MPa	**10524**	1625	0.15	
	$E_{3,h}$	MPa	**7701**	1502	0.19	
Fracture energy in compression for loading parallel to bed joints	$G_{f\text{-}c,h}$	N/mm	**12.8**	4.34	0.34	
Strain corresponding to peak strength in compression in the direction parallel to bed joints	$\varepsilon_{p,h}$	‰	**1.58**	0.39	0.24	
Masonry flexural strength with the moment vector parallel to the bed joints and in the plane of the wall	f_{x1}	MPa	**0.58**	0.08	0.14	5
Masonry flexural strength with the moment vector orthogonal to the bed joint and in the plane of the wall	f_{x2}	MPa	**0.73**	0.03	0.04	4
Masonry flexural strength with the moment vector orthogonal to the plane of the wall	f_{x3}	MPa	**0.41**	0.07	0.17	5
Flexural bond strength	f_w	MPa	**0.55**	0.09	0.17	20
Masonry (bed joint) initial shear strength	f_{v0}	MPa	**0.83**	-	-	11
Masonry (bed joint) shear friction coefficient	μ		**1.48**	-	-	

5 Testing protocol

In this section the testing protocol for the in-plane test is presented. First the test set-up is introduced. Second, the loading scheme is described. Third, the measurement system is reported.

5.1 Test set-up

Figure 2 shows the in-plane test set-up for slender and squat walls. The set-up has been designed in 2015 [5], making use of the steel-frame assembling system at the TU Delft in combination with the available anchor points in the strong concrete laboratory floor.
The set-up consists of horizontal and vertical actuators. The horizontal actuator has a capacity of 400 kN. For the pre-compression loading, four vertical actuators with a capacity of each 100 kN are used. The vertical actuators are loaded in tension and are positioned by a steel frame on the top steel beam. The vertical actuators are controlled pairwise, to ensure that the actuator load in each pair is the same. The vertical loading in the actuators could be differentiated to achieve two different boundary conditions: cantilever (shear span $H_0/H=1.0$) and double-clamped (shear span $H_0/H=0.5$) configuration. The actuator control is managed by software.

A frame composed by a bottom and a top steel beam and two lateral steel column is adopted for the construction, transportation and testing of the wall. In order to prevent sliding between the masonry and the steel supporting beams, the first and last masonry course is glued with “Sikadur 30”. Failure due to tensile bending stresses or shear failure can occur only in the masonry and not at the steel-masonry interface. The bottom steel beam is connected to cross-beams, which are anchored to the floor to prevent uplift. The top steel beam is used to introduce both the vertical and horizontal load to the masonry wall. The horizontal actuator is connected with steel tubes to the centre part of the top steel beam and induces a cyclic shear force on the test specimen. The out-of-plane rotation of the top beam is prevented by the frame that introduces the tension force of the vertical actuators (section B in Figure 2)

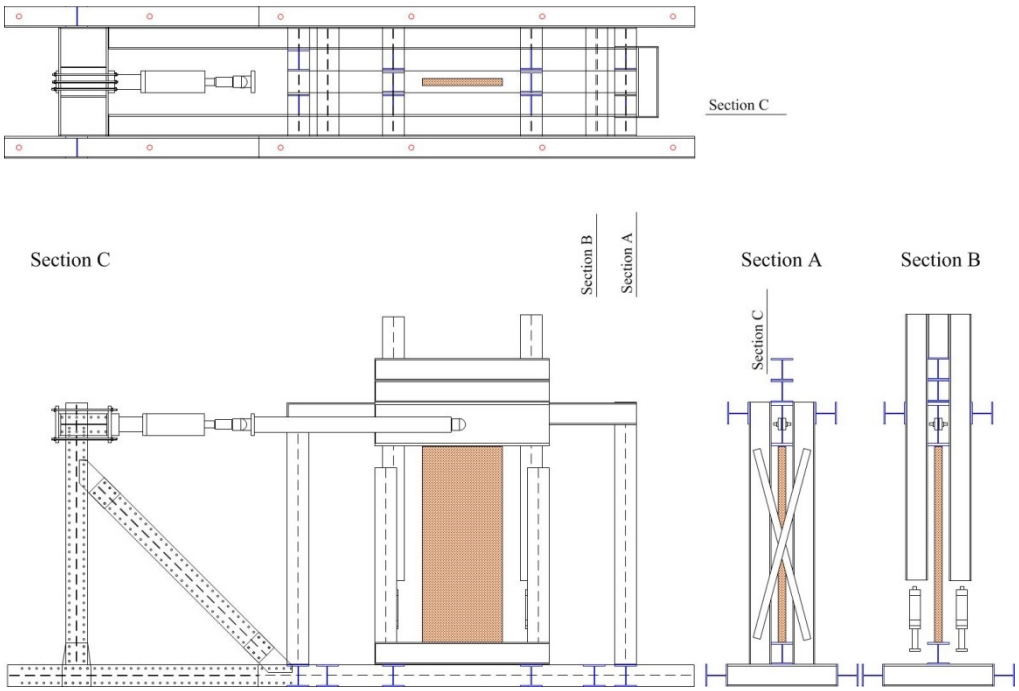

(a)

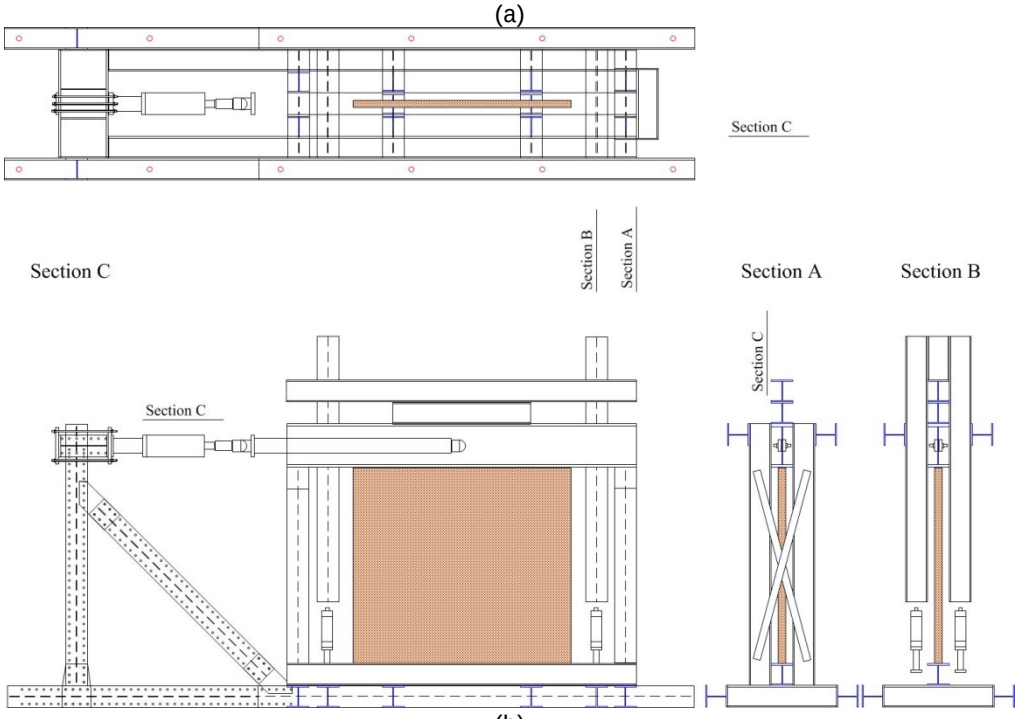

(b)

Figure 2 – In-plane test set-up for: (a) slender walls; (b) squat walls.

5.2 Loading scheme

During the in-plane test, the wall is subject to a shear-compression stress state following the loading scheme shown in Figure 3.

The displacement at the top of the wall is imposed with a horizontal actuator connected to the centre of the top steel beam, generating a horizontal force F_H. This force is imposed at a distance H_a from the base of the wall.

During the test the pre-compression load is controlled with vertical actuators placed at a distance d_1, which impose the forces F_R and F_L. In the case of a squat wall, a reduced lever arm d_2 ($d_2 < d_1$) is adopting as shown in Figure 3b. Thanks to this system, the force in the vertical actuator can be always positive (traction) even for large horizontal displacements.

Considering the set-up adopted to load the wall, the top steel beam system produce a constant load W_T given by the weight of the top spreading beams, the frame for the vertical actuators and half of the weight of tubular structure used to apply the horizontal load. The weight of the horizontal actuator W_E, placed at a distance d_3 for the centre of the wall, balanced by a counter weight.

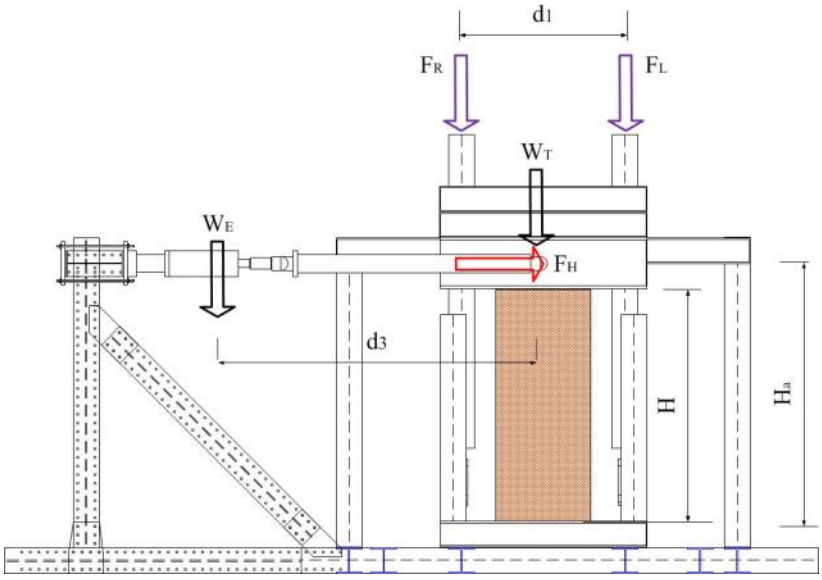

(a)

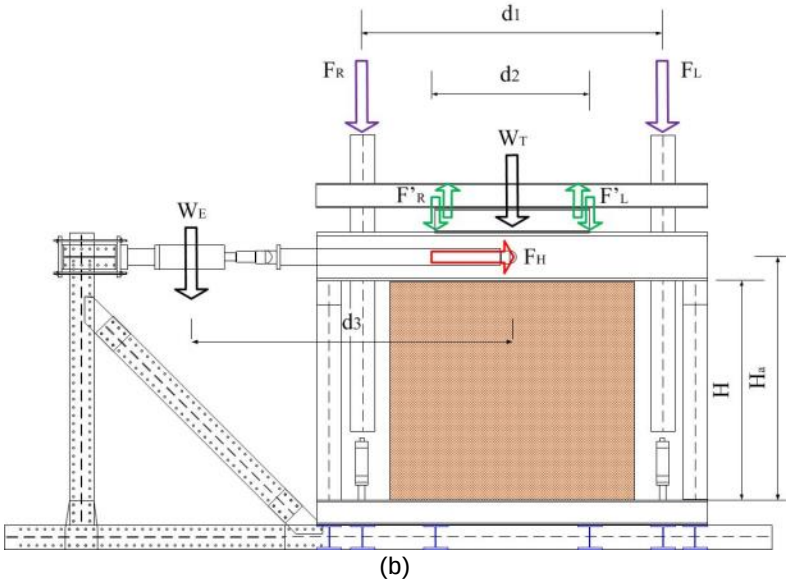

(b)

Figure 3 – Loading scheme for specimens subject to in-plane test: (a) slender wall; (b) squat wall.

The in-plane test can be performed applying two different boundary conditions following the cantilever or the double clamped configuration. In both configurations the wall is subjected to a cyclic horizontal displacement, while a pre-compression load σ_v at the top of the wall is kept. The horizontal displacement is cyclically applied. Every cycle is composed by three identical runs; in every run the desired horizontal target displacement is applied in both directions starting and ending at the zero position, which is the initial position of the wall. The horizontal loading is applied in the following steps:

- First, the desired pre-compression load P is applied through the vertical actuators (F_R and F_L), by considering the additional weight of the steel beam system W_T (Figure 3). The sum of the forces in the actuators will remain constant during the test.
- Second, a cycle C0F in force controlled is performed. The horizontal force is increased to reach approximatively 20% of the expected maximum force ($F_{H,20\%}$). The corresponding jack's displacement is measured.
- Three cycles namely C1D, C2D and C3D are applied in which the imposed jack's displacement is equal to 1, 2 and 3 times the measured displacement in cycle C0F.
- Eventually, a cyclic horizontal load is applied in displacement control by imposing an increment of the wall drift. In the initial phase, cycles are performed with a limited increase in drift (e.g. 0.025%) to capture the beginning of the nonlinear behaviour.

The test terminates once one of the following conditions is achieved:

- A displacement of 100 mm is reached in the horizontal actuator.
- A compression force in one of the vertical actuators is achieved (during double clamped configuration).
- A degradation of 20% of the maximum resistance of the walls is reported.
- A safety hazard is verified due to extensive damage.

During the application of the horizontal displacement, the pre-compression load P is kept constant. Different loading conditions are imposed to the vertical actuators in order to simulate the two different types of boundary conditions.

In the case of **cantilever configuration**, the forces in the actuators are related with the following equations:

$$\begin{cases} F_R + F_L + W_T = P \\ F_R - F_L = 0 \end{cases} \tag{1}$$

where F_R and F_L are the forces in the right and left actuators, respectively. On both sides, two actuators are placed, which are coupled in order to have the same force.

From Eq. (1), the forces in the vertical actuators can be determined as:

$$F_R = F_L = \frac{P - W_T}{2} \tag{2}$$

The vertical force F_R and F_L remained constant during the test and they are independent on the horizontal force F_H.

In the case of **double-clamped configuration**, it is imposed that the pre-compression force on top of the wall is constant and the rotation of the top edge of the wall is restrained. The following conditions are applied

$$\begin{cases} F_R + F_L + W_T = P \\ v_R = v_L \end{cases} \tag{3}$$

where v_R and v_L are the vertical displacements measured between the top and bottom steel beams, which are glued on the masonry wall (measured by sensors FR5 and FR6 in Figure 4). In order to have a uniform displacement at the top of the wall, the displacement v_R and v_L in the vertical actuators are dynamically updated during the test. Consequently, the force F_R and F_L are dynamically updated during the test according to the "kinematic" criterion, and they are related to the horizontal force F_H.

5.3 Instrumentation

The measurement system has been designed to:

- record the applied vertical and horizontal force on the wall;
- record the net horizontal and vertical deformations at the top of the wall;
- record the local deformations at the top and bottom side of the wall (crack opening at the corner and sliding over the first and last mortar bed joint)
- record the evolution of the crack pattern;

Figure 4 shows the measurement system adopted for the in-plane tests on large-scale walls. An indication of the intended measurement, the sensor type and the maximum stroke in both directions from the centre position of each measurement point is given in Table 7.

At the back side of the wall (section C) a measurement system is used by employing linear potentiometers and lasers. The net horizontal and net vertical displacements at the top of the wall are computed through the vertical (sensors 1-4) and diagonal (sensors 5-6) measurements. The net horizontal displacement can be different from the jack's displacement, especially for small values. Additionally, the displacement of the top and bottom steel beams are monitored with respect to an external reference system using sensors 19-20. Sliding of the wall at the top and bottom side is monitored with sensors 7-10, while sensor 11 reports horizontal deformation at the centre of the wall. The cracking/crushing mechanisms that can occur at the corners of the wall due to flexural deformations are monitored with sensors 12-15. The sensors are installed over a length of 5 bricks. The absence of undesired out-of-plane deformation of the wall during the tests is monitored through the measurement points 16-18. The forces are measured with load cells placed next to the hydraulic jacks (sensors 21-22). To evaluate possible deformation of the set-up, the vertical displacement of the top flange of the bottom HEB300 beam, on which the wall is glues, is monitored with respect to the floor (sensors FR1-FR4). Making use of the sensors 19, 20 and FRs, another estimation of the horizontal displacement of the wall can be obtained, which here is named frame displacement. The front side of the wall is equipped for photogrammetry measurement.

In this report the following conventions are adopted:

- The front-right side of the wall, named also 12 side, is the one closer to the horizontal actuator.
- The front-left side of the wall, named also 34 side, is the one far to the horizontal actuator.
- The positive displacement/force corresponds to a deformation from right to left of the wall
- The negative displacement/force corresponds to a deformation from left to right of the wall
- In a run, the first imposed displacement is always negative.

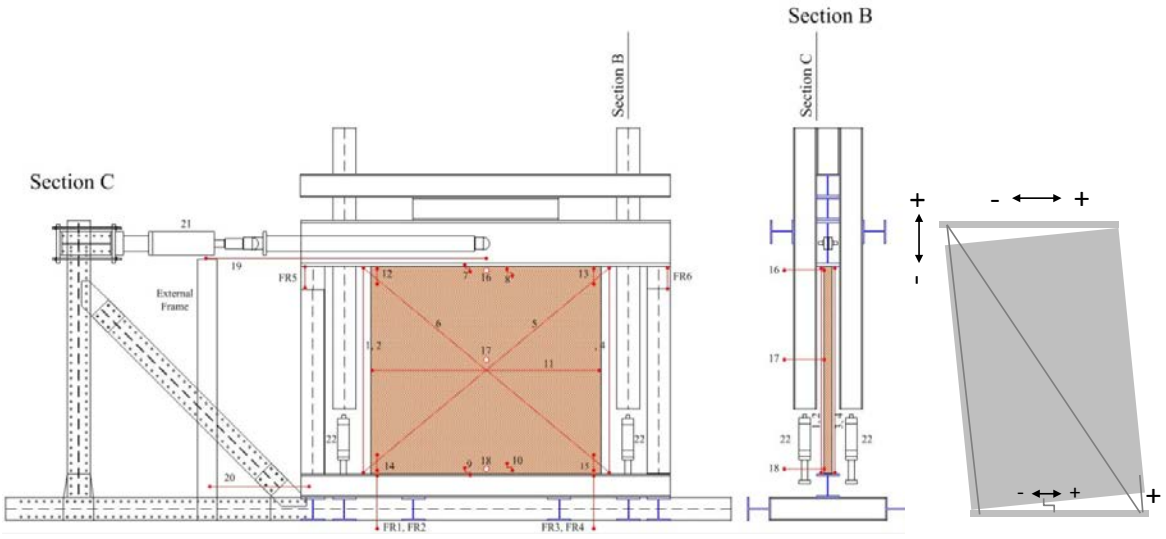

(a) (b)

Figure 4 – Measuring system adopted for in-plane tests on the back side of the wall and signs' convention.

Table 7 - Overview of the measuring points and sensor types used in the in-plane tests.

No.	Description	Sensor Type	Stroke (mm)
1	Vertical displacement between top and bottom steel beam (front-right side)	Linear potentiometer	+/-100
2	Vertical displacement between top and bottom steel beam (back-right side)	Linear potentiometer	+/-100
3	Vertical displacement between top and bottom steel beam (back-left side)	Linear potentiometer	+/-100
4	Vertical displacement between top and bottom steel beam (front-left side)	Linear potentiometer	+/-100
5	Diagonal displacement between steel beams (back side)	Linear potentiometer	+/-50
6	Diagonal displacement between steel beams (back side)	Linear potentiometer	+/-50
7	Horizontal displacement between steel beam and first brick layer at the top of the wall (back side)	Linear potentiometer	+/-10
8	Horizontal displacement between the first and the second brick layer at the top of the wall (back side)	Linear potentiometer	+/-10
9	Horizontal displacement between steel beam and first brick layer at the bottom of the wall (back side)	Linear potentiometer	+/-10
10	Horizontal displacement between the first and the second brick layer at the bottom of the wall (back side)	Linear potentiometer	+/-10
11	Horizontal displacement at mid-height of the wall (front side)	Linear potentiometer	+/-25
12	Vertical displacement over 4 bricks at the top left corner (back side)	Linear potentiometer	+/-25
13	Vertical displacement over 4 bricks at the top right corner (back side)	Linear potentiometer	+/-25
14	Vertical displacement over 4 bricks at the bottom left corner (back side)	Linear potentiometer	+/-25
15	Vertical displacement over 4 bricks at the bottom right corner (back side)	Linear potentiometer	+/-50
16	Out-of-plane displacement at the top of the wall (back side, middle length)	Laser	+/-100
17	Out-of-plane displacement at mid-height of the wall (back side, middle length)	Laser	+/-100
18	Out-of-plane displacement at the bottom of the wall (back side, middle length)	Laser	+/-100
19	Horizontal displacement top steel beam (for large displacement)	Linear potentiometer	+/-100
19a	Horizontal displacement top steel beam (for small displacements)	Laser	+/-25
20	Horizontal displacement bottom steel beam	Linear potentiometer	+/-100
21	Horizontal actuator 400 kN – load and displacement	Load cell and HBM LVDT	+/-100
22	Vertical actuator 100 kN (4x)-load and displacement	Load cell and HBM LVDT	+/-20
23	Measure points for photogrammetry (front side)	stickers	
FR1-FR4	Vertical displacement of the bottom steel beam with respect to the floor	Linear potentiometer	+/-10
FR5-FR6	Vertical displacement between top beam and columns (used by the control system during double clamped configuration)	Linear potentiometer	+/-100

6 Experimental results

In this Section the experimental results for each wall are reported in terms of capacity curve, initial stiffness, drift, energy dissipated and crack pattern. The capacity curve and the drift are defined on the basis of the net horizontal displacement calculated with the measurements of sensors 1 to 6. The drift d_r is the ratio between the net horizontal displacement and the height of the wall H_w.

6.1 CS brick masonry wall (TUD_COMP-20)

The wall TUD_COMP-20, made in calcium silicate bricks masonry, was tested under cantilever configuration with a pre-compression load of 0.63 MPa. The test was performed in 18 cycles. In the first cycle C0F, a force of 2 kN was applied and a jack's displacement of +/- 0.4 mm was measured. In the following three cycles (C1D, C2D and C3D) a jack's displacement equal to 1, 2 and 3 times the measured displacement was applied. Subsequently, increments in drift were applied. In cycle C13, the maximum capacity of the jack was reached; although the force reduction was substantial cycle C14 was performed in which the same displacement of cycle C13 is imposed. In Table 8 the complete loading history is reported.

Table 8 – Loading history for wall TUD_COMP-20.

Cycle	Net displacement		Drift	
	mm		%	
C1D	-0.03	0.03	0.001	0.001
C2D	-0.17	0.14	-0.01	0.01
C3D	-0.64	0.50	-0.02	0.02
C1	-0.67	0.47	-0.02	0.02
C2	-1.58	1.14	-0.06	0.04
C3	-2.70	2.19	-0.10	0.08
C4	-3.88	3.34	-0.14	0.12
C5	-8.77	8.10	-0.32	0.29
C6	-18.63	17.84	-0.67	0.64
C7	-28.75	27.62	-1.03	0.99
C8	-38.86	37.35	-1.40	1.34
C9	-48.73	47.18	-1.75	1.70
C10	-58.66	56.93	-2.11	2.05
C11	-68.95	68.13	-2.48	2.45
C12	-80.13	78.53	-2.88	2.82
C13	-86.87	86.33	-3.12	3.11
C14	-86.39	87.06	-3.11	3.13

Figure 5 shows the in-plane behaviour of wall TUD_COMP-20 in terms of capacity curve and drift, while Figure 6 shows the relation between the net vertical and net horizontal displacement. The initial stiffness of the wall was estimated in cycle C2D and it is equal to K = 17 kN/mm. The wall TUD_COMP-20 shows a maximum bases shear force of +15.37 and -14.75 kN in the positive and negative loading direction, respectively. After the maximum base share force was achieved, a gradual reduction in force occurred with substantial energy dissipation. A 20% reduction in base shear force was reached at a displacement of +68.1 and -69.1 mm for positive and negative loading direction, respectively. The wall was subject to a maximum displacement of 87 mm, corresponding to a drift of 3.1% (Figure 5b), until collapse occurred.

The damage was mainly localised in the bottom part of the specimen (Figure 7). Horizontal cracks subsequently developed in the three mortar bed joints at the bottom of the wall. Thanks to the gradual development of these cracks, the wall was subject to pure rocking movement and its effective height was gradually reduced. For large displacement, splitting cracks at the bottom-left and bottom-right corner of the wall occurred, by leading to detachment of masonry portions (Figure 7b). In cycle C13 and C14, where the same displacement was applied, the phenomenon of toe crushing could be observed (Figure 8); the base shear force substantially for the same imposed displacement. This phenomenon led to instability of the wall for large displacement and its collapse (Figure 7c). Figure 9 show the energy dissipated during the test.

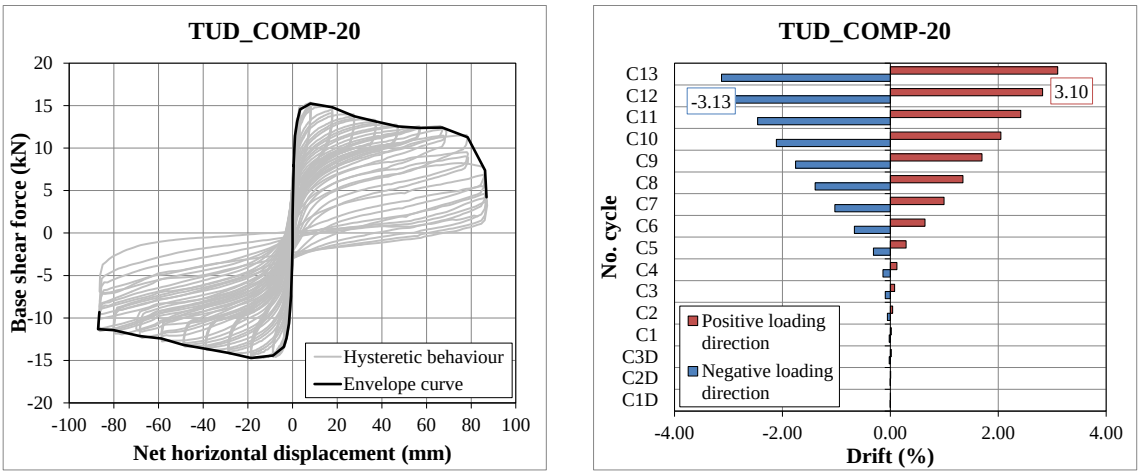

(a) (b)

Figure 5 – In-plane behaviour of wall TUD_COMP-20: (a) Capacity curve; (b) Drift.

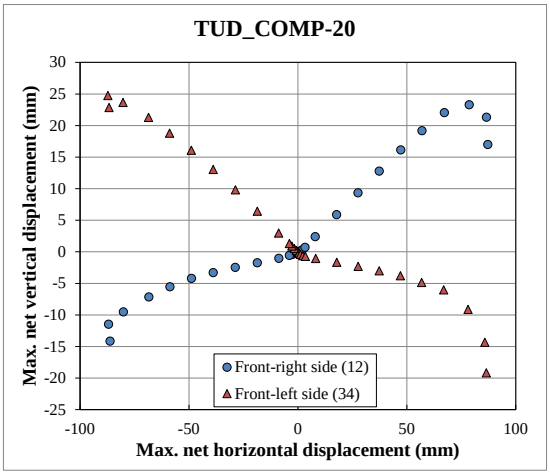

Figure 6 – Maximum net vertical versus horizontal displacement for wall TUD_COMP-20.

(a) (b)

Figure 7 – Crack pattern of wall TUD_COMP-20: (a) Just before collapse; (c) At collapse.

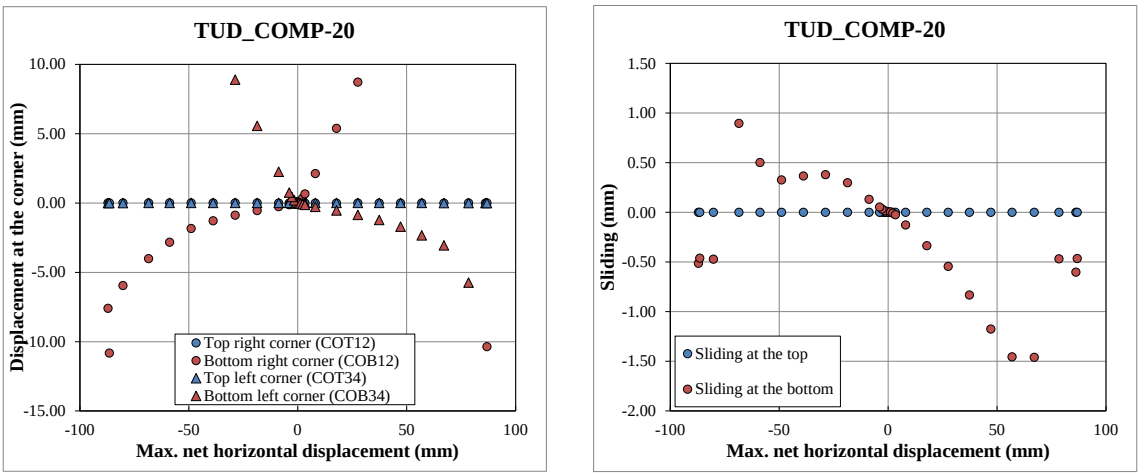

(a) (b)

Figure 8 – Local deformation for wall TUD_COMP-20: (a) Crushing at the corners; (b) Sliding.

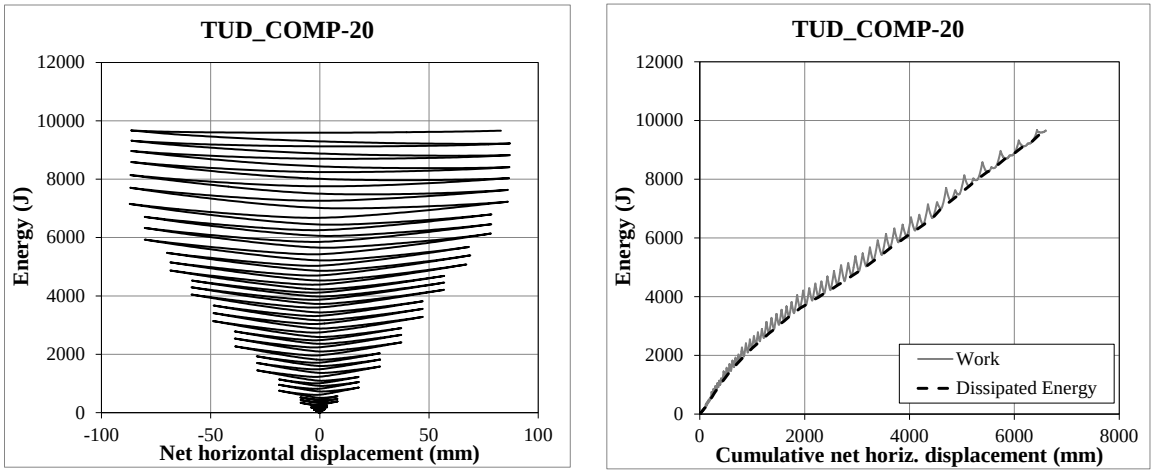

(a) (b)

Figure 9 – Energy dissipation for wall TUD_COMP-20: (a) Energy vs. net horizontal displacement; (b) Work and dissipated energy vs. cumulative net horizontal displacement.

6.2 Solid clay brick masonry walls (TUD_COMP-21, -22, -23)

Three walls in solid clay brick masonry were tested: one wall in single wythe masonry (TUD_COMP-21) and two walls in double wythe masonry (TUD_COMP-22 and TUD_COMP-23).

6.2.1 Wall TUD_COMP-21

The wall TUD_COMP-21 in single wythe masonry was tested with the purpose to investigate shear failure in walls made of clay brick masonry. The wall was tested under double-clamped configuration with a pre-compression load of 0.34 MPa. The test was performed in 8 cycles. In the first cycle C0F, a force of 15 kN was applied and a jack's displacement of 1.1 mm was measured. In the following three cycles (C1D, C2D and C3D) a jack's displacement equal to 1, 2 and 3 times the measured displacement was applied. Subsequently, increments in drift were applied. In Table 9 the complete loading history is reported in terms of net displacement and corresponding drift.

Table 9 – Loading history for wall TUD_COMP-21.

Cycle	Net displacement		Drift	
	mm		%	
C1D	-0.01	0.02	-0.0005	0.001
C2D	-0.12	0.06	-0.004	0.002
C3D	-0.22	0.34	-0.01	0.01
C1	-0.42	0.23	-0.02	0.01
C2	-3.65	3.54	-0.14	0.13
C3	-7.67	7.24	-0.28	0.27
C4	-12.62	10.57	-0.47	0.39

Figure 10 shows the in-plane behaviour of wall TUD_COMP-21 in terms of capacity curve and drift, while Figure 11 shows the relation between the net vertical and net horizontal displacement. The initial stiffness of the wall was estimated in cycle C2D and it is equal to K = 160.6 kN/mm. The wall TUD_COMP-21 shows a maximum bases shear force of +97.20 and -98.95 kN in the positive and negative loading direction, respectively. In cycle C2, the maximum base shear force is reached together with the starts of the dissipative behaviour (Figure 12); at this stage the formation of the diagonal cracks occurred. In the following cycles, although only an increment in 0.25% of drift was applied a substantial reduction in forced was obtained. A 20% reduction in base shear force was reached at a displacement of +3.2 and -3.1 mm for positive and negative loading direction, respectively. The wall was subject to a maximum displacement of 12 mm, corresponding to a drift of 0.47% (Figure 10b).

The typical shear failure composed by two diagonal cracks occurred (Figure 13). The formation of step-wise cracks in the bed and head joint occurred in the central part of the wall, while at the corners the diagonal crack occurred also in the bricks. In the corners, it is possible to observe that the last and first brick courses, which are glued on the steel beams, were also damaged. Consequently, the two triangular portion of masonry on the left and right hand side of the wall created by the diagonal cracks results detached from the rest of the wall. This caused the formation of residual deformation in the net horizontal displacement of the wall in cycle C3 and C4.

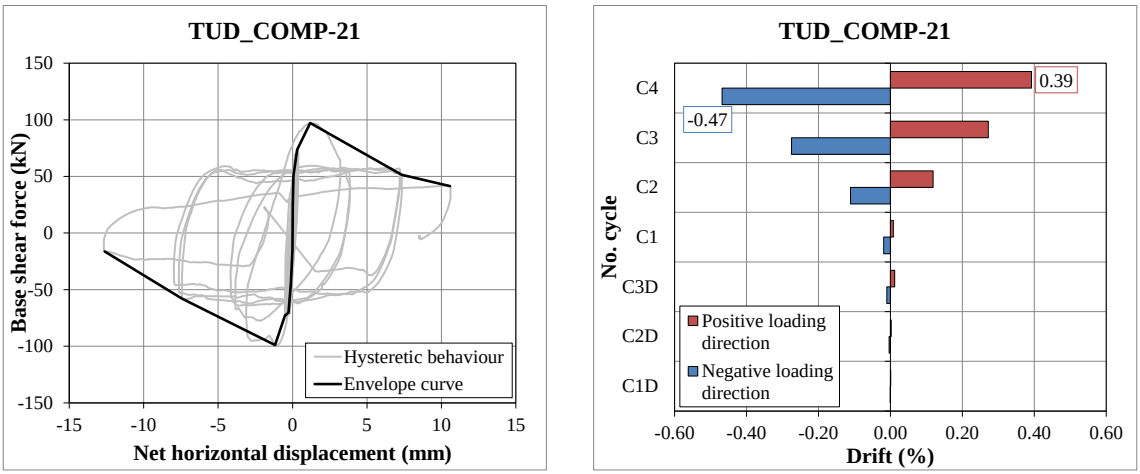

(a) (b)

Figure 10 – In-plane behaviour of wall TUD_COMP-21: (a) Capacity curve; (b) Drift.

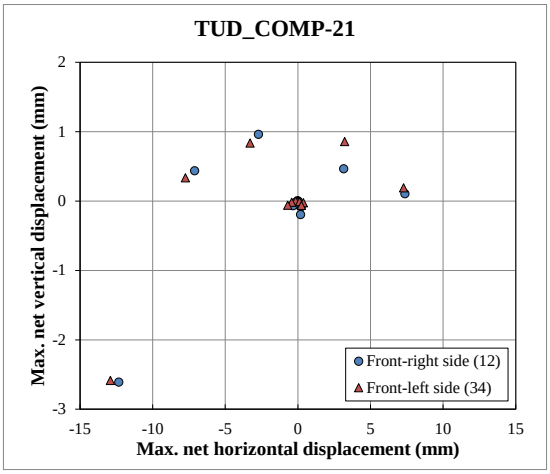

Figure 11 – Maximum net vertical versus horizontal displacement for wall TUD_COMP-21.

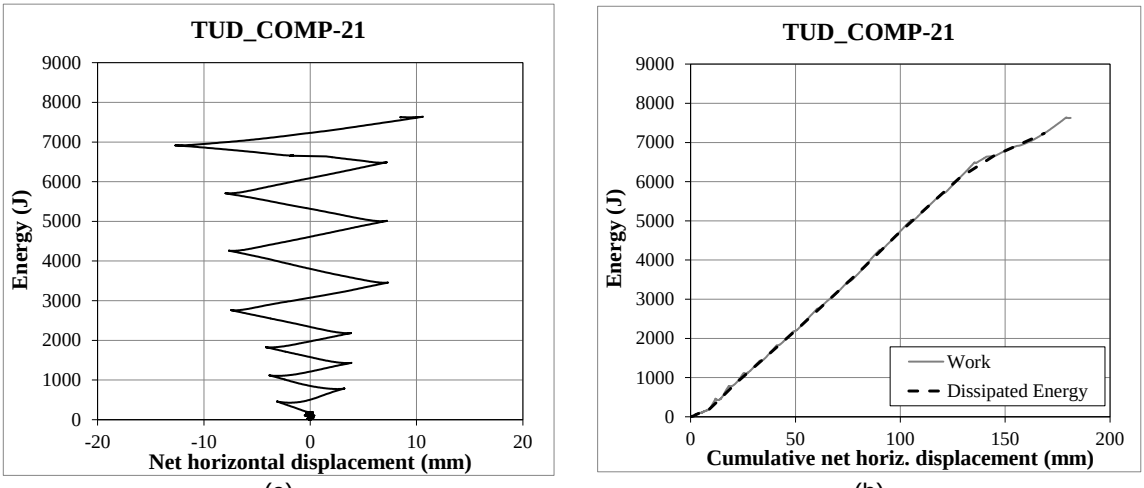

(a) (b)

Figure 12 – Energy dissipation for wall TUD_COMP-21: (a) Energy vs. net horizontal displacement; (b) Work and dissipated energy vs. cumulative net horizontal displacement..

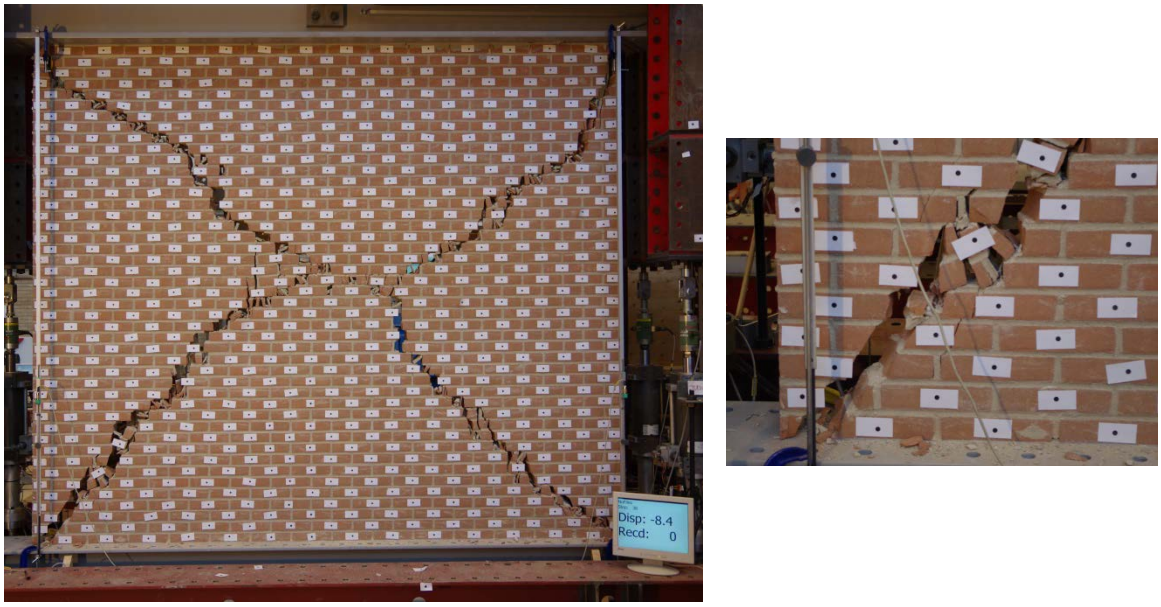

(a) (b)

Figure 13 – Crack pattern of wall TUD_COMP-21 at the end of the test: (a) Overview; (b) Detail bottom-left corner.

6.2.2 Wall TUD_COMP-22

The wall TUD_COMP-22 in double wythe solid clay brick masonry was tested under cantilever configuration with a pre-compression load of 0.34 MPa. The test was performed in 12 cycles. In the first cycle C0F, a force of 22 kN was applied and a jack's displacement of 1.4 mm was measured. In the following three cycles (C1D, C2D and C3D) a jack's displacement equal to 1, 2 and 3 times the measured displacement was applied. Subsequently, increments in drift were applied. In Table 10 the complete loading history is reported in terms of net displacement and corresponding drift.

Table 10 – Loading history for wall TUD_COMP-22.

Cycle	Net displacement		Drift	
	mm		%	
C1D	-0.02	0.01	-0.0008	0.0004
C2D	-0.14	0.07	-0.01	0.003
C3D	-0.27	0.25	-0.01	0.01
C1	-2.81	3.49	-0.10	0.13
C2	-6.99	7.51	-0.26	0.28
C3	-19.46	18.36	-0.72	0.68
C4	-28.59	26.51	-1.06	0.98
C5	-41.00	40.73	-1.52	1.51
C6	-41.85	43.29	-1.55	1.60
C7	-50.06	44.59	-1.85	1.65
C8	-50.07	49.11	-1.85	1.82

Figure 14 shows the in-plane behaviour of wall TUD_COMP-22 in terms of capacity curve and drift, while Figure 15 shows the relation between the net vertical and net horizontal displacement. The initial stiffness of the wall was estimated in cycle C2D and it is equal to K = 162.3 kN/mm. The wall TUD_COMP-22 shows a maximum base shear force of +116.71 and -117.70 kN in the positive and negative loading direction, respectively. A 20% reduction in base shear force was reached only for the positive loading direction at a displacement of +49.1 mm. The wall was subject to a maximum displacement of 50 mm, corresponding to a drift of 1.85%.

The wall showed a hybrid failure consisting in bed joint sliding at the bottom of the wall followed by crushing at the bottom-left corner (Figure 16). The formation of a horizontal crack at the first and second mortar bed joints occurred cycle C1 (d_r = 0.1%). Figure 17a shows the local deformation measured by sensors 12-16 at the top and bottom corners; positive value can be interpreted as a measurement of crack opening, while negative values indicate crushing. The sliding of the wall over the first mortar bed joint was substantial (Figure 17b) leading to a difference between the jack's and the net displacements. The degradation of the capacity and the dissipation of energy (Figure 18) substantially increased in the last cycles due to the crushing at the bottom-left corner.

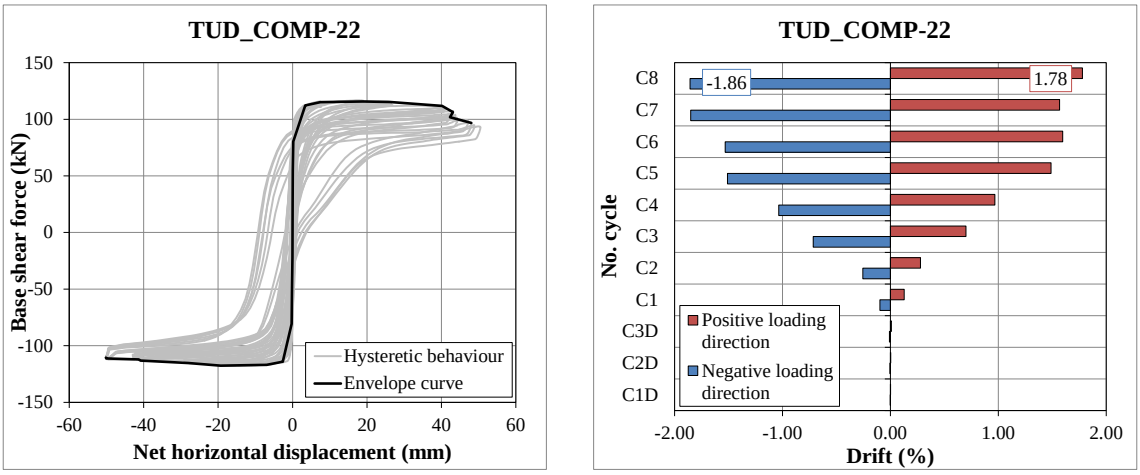

(a) (b)

Figure 14 – In-plane behaviour of wall TUD_COMP-22: (a) Capacity curve; (b) Drift.

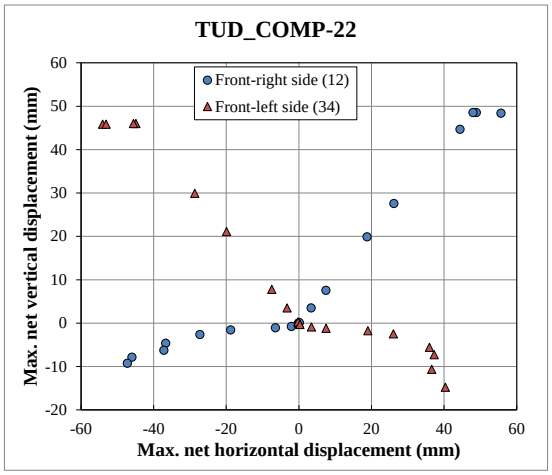

Figure 15 – Maximum net vertical versus horizontal displacement for wall TUD_COMP-22.

(a) (b)

Figure 16 – Crack pattern of wall TUD_COMP-22 at the end of the test: (a) Overview; (b) Detail.

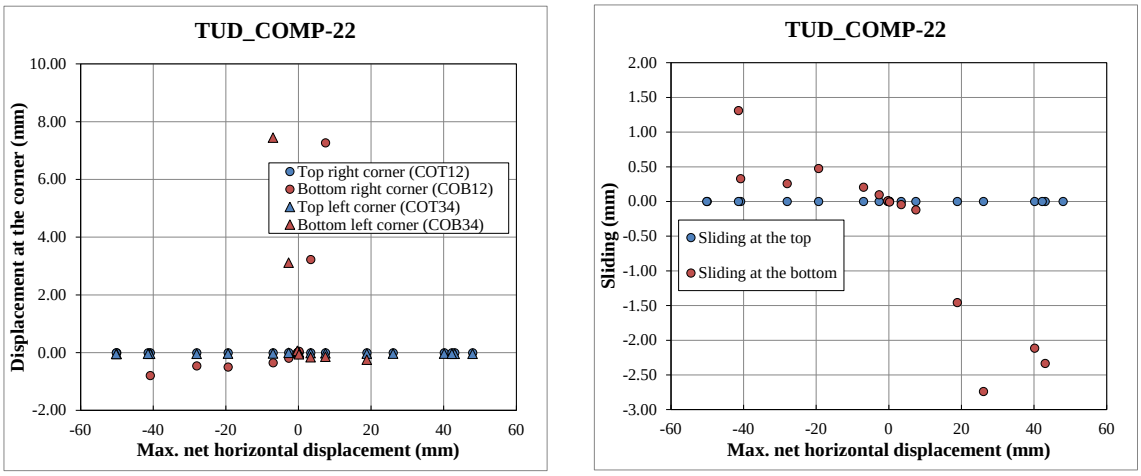

(a) (b)

Figure 17 – Local deformation for wall TUD_COMP-22: (a) Crack opening and crushing; (b) Sliding.

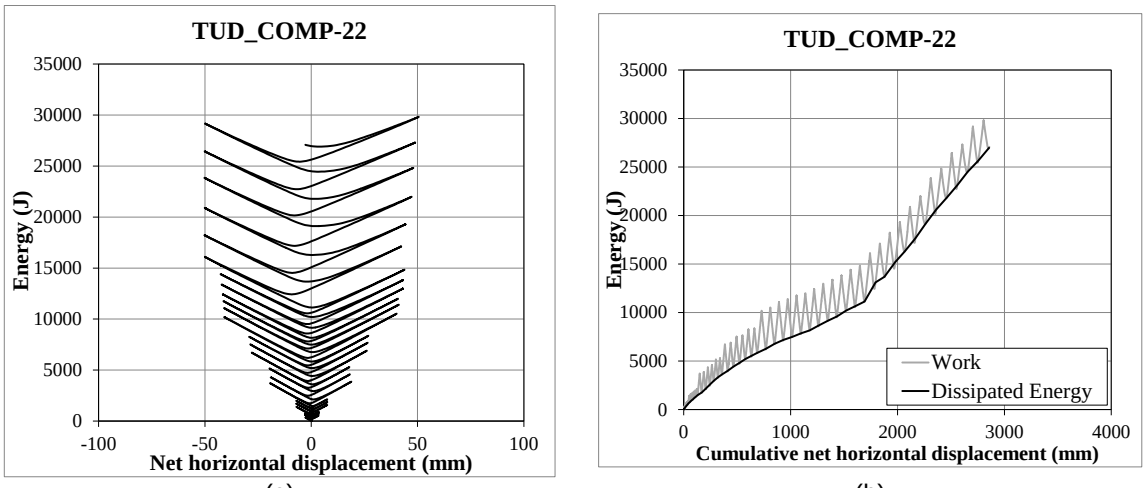

(a) (b)

Figure 18 – Energy dissipation for wall TUD_COMP-22: (a) Energy vs. horizontal displacement; (b) Work and dissipated energy vs. cumulative displacement.

6.2.3 Wall TUD_COMP-23

The wall TUD_COMP-23 was similar in geometry and boundary conditions to the wall TUD_COMP-22, but an asymmetrically placed opening was present. The wall was made of double wythe solid clay brick masonry and it was tested under cantilever configuration with a pre-compression load of 0.34 MPa. The test was performed in 9 cycles. In the first cycle C0F, a force of 22 kN was applied and a jack's displacement of 1.6 mm was measured. In the following three cycles (C1D, C2D and C3D) a jack's displacement equal to 1, 2 and 3 times the measured displacement was applied. Subsequently, increments in drift were applied. In Table 11 the complete loading history is reported in terms of net displacement and corresponding drift.

Table 11 – Loading history for wall TUD_COMP-23.

Cycle	Net displacement		Drift	
	mm		%	
C1D	-0.03	0.04	-0.001	0.002
C2D	-0.17	0.50	-0.01	0.02
C3D	-0.94	1.42	-0.03	0.05
C1	-4.27	5.39	-0.16	0.20
C2	-8.59	9.85	-0.32	0.36
C3	-22.93	23.91	-0.85	0.88
C4	-26.04	26.60	-0.96	0.98
C5	-33.05	23.09	-1.22	0.85

Figure 19 shows the in-plane behaviour of wall TUD_COMP-23 in terms of capacity curve and drift, while Figure 20 shows the relation between the net vertical and net horizontal displacement. The initial stiffness of the wall was estimated in cycle C2D and it is equal to K =66.6 kN/mm. The wall TUD_COMP-23 shows a maximum base shear force of +85.37 and -108.92 kN in the positive and negative loading direction, respectively. A 20% reduction in base shear force was reached only for the negative loading direction at a displacement of -28.5 mm. The wall was subject to a maximum displacement of +23.1 and -33.1 mm, corresponding to a drift of +0.85 and -1.22%, for the positive and negative loading direction respectively. The asymmetric behaviour in terms of force and displacement capacity can be explained by the damage evolution.

The integrity of the wall was gradually loss due to failing of the lintel and formation of two separate piers (Figure 22). In the top part of the wall, diagonal step-wise cracks formed, starting from the lintel. On the contrary, in the bottom part of the wall two type of crack formed both of them starting from the opening corner: one horizontal crack and one step-wise crack. On the basis of the loading direction, the horizontal or the step-wise crack at the bottom of the wall were open, as shown in Figure 22c. In the pre-peak phase (cycle C3, Figure 22a,b), the portion of masonry above the opening was cooperating with one pier on the basis of the loading direction. After the failure in bending of the masonry lintel (cycle C4/C5, Figure 22c,d), two separate piers were visible. The top part of masonry between the lintel and the steel beam was sliding together with the top steel beam, being glued on it. After the failure of the front part of the lintel, nearly any horizontal displacement was observed for the wide pier on the front-left of the wall. This was caused by a progressive sliding of the timber beam, which was positioned on the back part of the lintel.

Figure 21 shows the energy dissipated during the test. It is possible to note that the failure of the lintel and the change in mechanism lead to a sudden increase in dissipated energy.

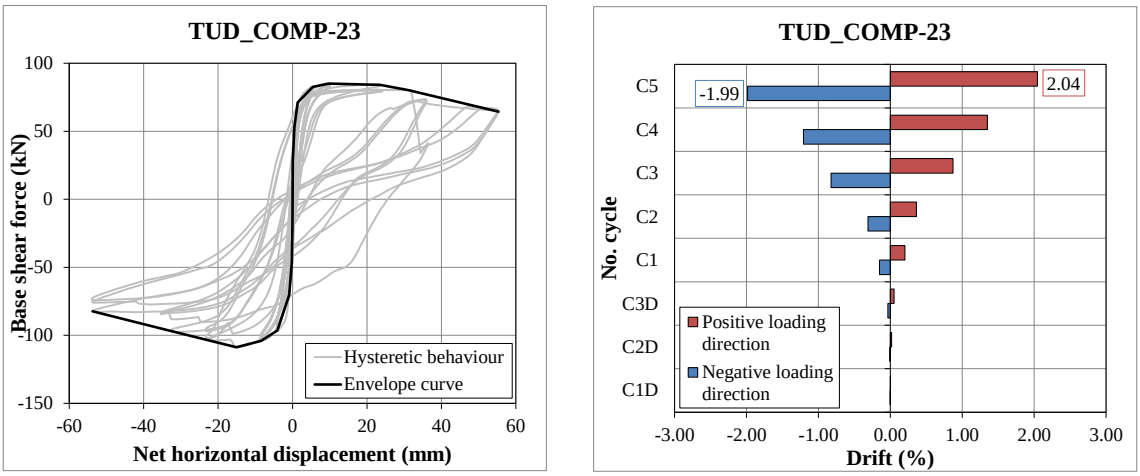

(a) (b)

Figure 19 – In-plane behaviour of wall TUD_COMP-23: (a) Capacity curve; (b) Drift.

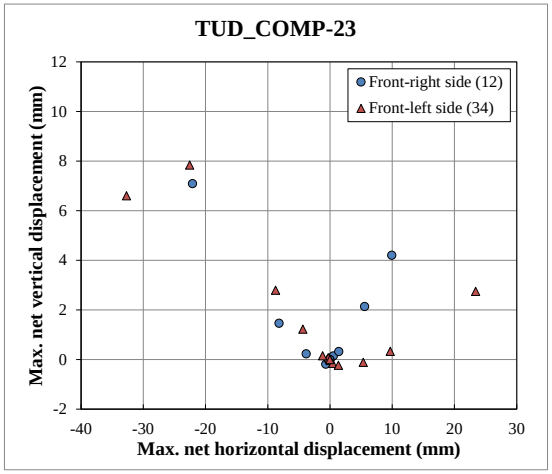

Figure 20 – Maximum net vertical versus horizontal displacement for wall TUD_COMP-23.

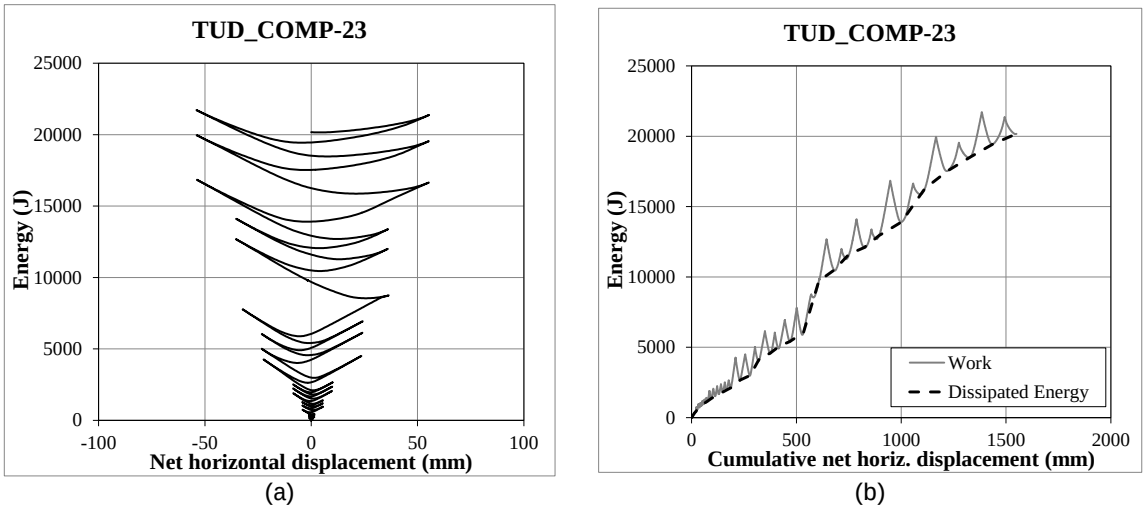

(a) (b)

Figure 21 – Energy dissipation for wall TUD_COMP-23: (a) Energy vs. net horizontal displacement; (b) Work and dissipated energy vs. cumulative net horizontal displacement.

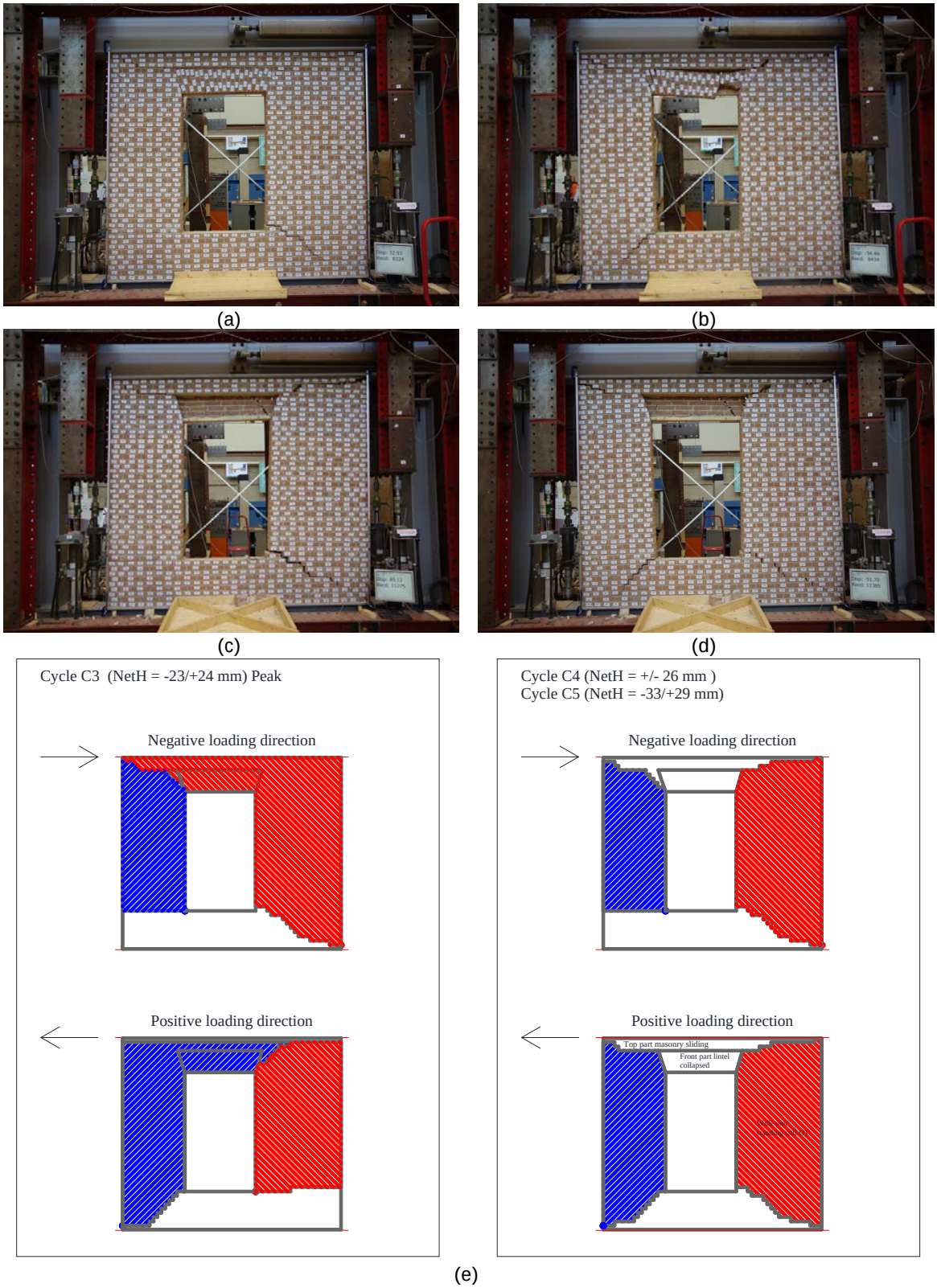

Figure 22 – Crack pattern of wall TUD_COMP-23 at the end of the test: (a)-(b) Crack pattern at failure of the lintel (cycle C4); (c)-(d) Crack pattern after failure of the lintel (cycle C5); (e) Overview.

6.3 CS element masonry walls (TUD_COMP-24, -25)

Two walls in calcium silicate element masonry were tested: one wall under cantilever configuration (TUD_COMP-25) and one wall under double-clamped configuration (TUD_COMP-24). The two walls had the same geometry and the same pre-compression load equal to 0.60 MPa.

6.3.1 Wall TUD_COMP-24

The wall TUD_COMP-24, made in CS element masonry, was tested under double clamped configuration with a pre-compression load of 0.60 MPa. The test was performed in 17 cycles. In the first cycle C0F, a force of 4 kN was applied and a jack's displacement of +/- 0.6 mm was measured. In the following three cycles (C1D, C2D and C3D) a jack's displacement equal to 1, 2 and 3 times the measured displacement was applied. Subsequently, increments in drift were applied. In Table 12 the complete loading history is reported in terms of net horizontal displacement and corresponding drift. Due to the detachment of vertical and diagonal sensors (sensors 1-6 in Figure 4), the net displacement of the wall in cycle C12 and C13 was calculated with respect to the relative displacement of the wall frame (sensors 19, 20 and FRs in Figure 4).

Table 12 – Loading history for wall TUD_COMP-24.

Cycle	Net displacement		Drift	
	mm		%	
C1D	-0.06	0.01	0.00	0.00
C2D	-0.18	0.11	-0.01	0.00
C3D	-0.50	0.27	-0.02	0.01
C1	-0.54	0.26	-0.02	0.01
C2	-0.89	0.48	-0.04	0.02
C3	-1.84	1.51	-0.07	0.05
C4	-2.86	2.50	-0.11	0.09
C5	-6.61	6.12	-0.24	0.22
C6	-8.67	8.10	-0.32	0.29
C7	-15.60	14.54	-0.58	0.48
C8	-20.98	16.39	-0.76	0.60
C9	-27.23	23.20	-1.00	0.84
C10	-33.70	29.98	-1.23	1.10
C11	-40.17	36.85	-1.47	1.35
C12*	-49.65	49.62	-1.82	1.82
C13*	-66.45	66.75	-3.45	1.53
* Displacement calculated from sensors 19, 20 and FRs				

Figure 23 shows the in-plane behaviour of wall TUD_COMP-24 in terms of capacity curve and drift, while Figure 24 shows the relation between the net vertical and net horizontal displacement. The initial stiffness of the wall was estimated in cycle C2D and it is equal to K = 42.79 kN/mm. The wall TUD_COMP-24 shows a maximum base shear force of +21.62 and -21.46 kN in the positive and negative loading direction, respectively. In the post-peak phase, limited degradation in force could be observed that did not result in a change of energy dissipation mechanism (Figure 25). A 50% reduction in base shear force was suddenly reached in cycle C13. After this reduction the test was stopped due to instability of the specimen. A maximum drift of -3.45 and +1.82% was reached in the negative and positive loading direction, respectively.

The wall TUD_COMP-24 showed an initial pure rocking mechanism followed by sliding over the bed joint and splitting failure at one corner. The first cracks occurred in the first and last mortar bed joint during cycle C3 (d_r = 0.06%); this damage allowed the pure rocking deformation of the wall. Figure 26a shows the crack opening at the corners (sensors 12-15) measured between the kicker layer and the first masonry course, while Figure 26b shows the sliding (sensors 8-9) between the kicker layer and the masonry measured at approximatively half of the wall's length. Due to the high slenderness ratio of the wall, an out-of-plane rotation of the wall occurred which resulted in a misaligned between the wall and the kicker layer. In cycle C13 the main damage occurred in a rapid sequence (Figure 27). First sliding over the mortar joint occurred in the first two courses. Afterwards, vertical cracks in the element occurred in the two courses. Eventually, splitting over the thickness of the smallest element unit at the bottom course occurred with consequent loss

of part of it. By analysing the damage evolution together with the capacity curve in Figure 27a, it is possible to note that the 50% reduction in base shear force was caused by cracking in the elements (Point C in Figure 27a), while the splitting of the bottom unit occurred in the second run at the maximum negative displacement (Point D in Figure 27a).

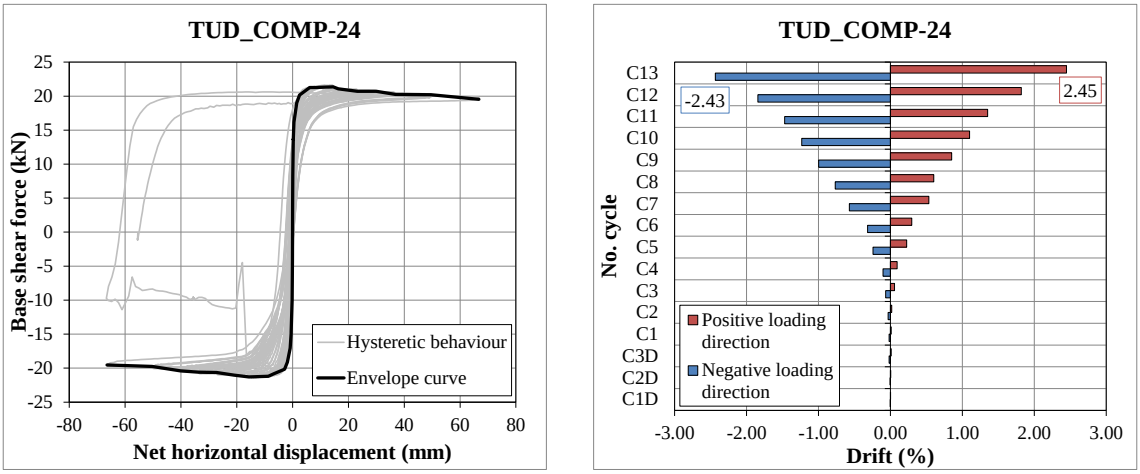

(a) (b)

Figure 23 – In-plane behaviour of wall TUD_COMP-24: (a) Capacity curve; (b) Drift.

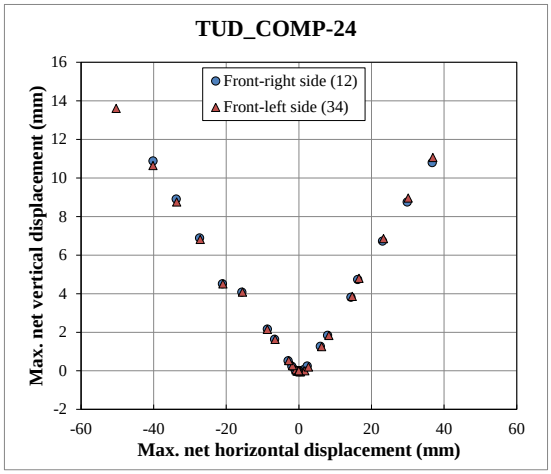

Figure 24 – Vertical versus horizontal displacement for wall TUD_COMP-24.

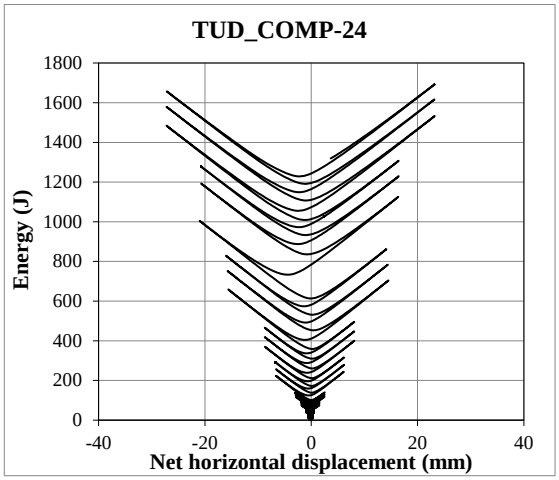

(a)

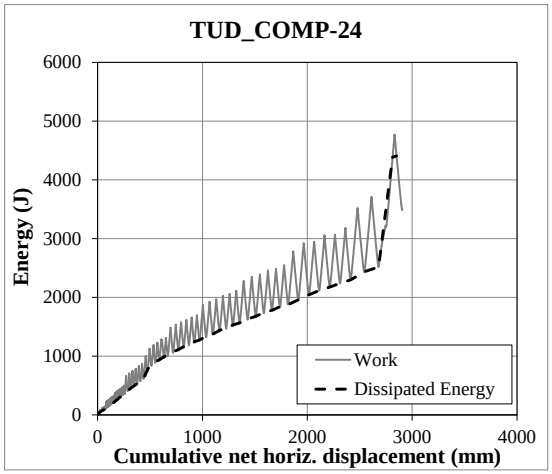

(b)

Figure 25 – Energy dissipation for wall TUD_COMP-24: (a) Energy vs. net horizontal displacement; (b) Work and dissipated energy vs. cumulative net horizontal displacement.

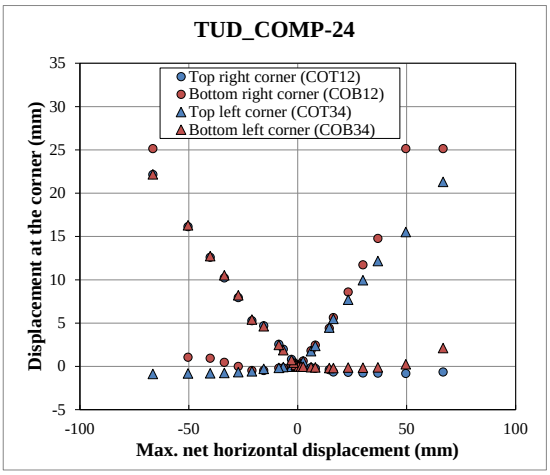

(a)

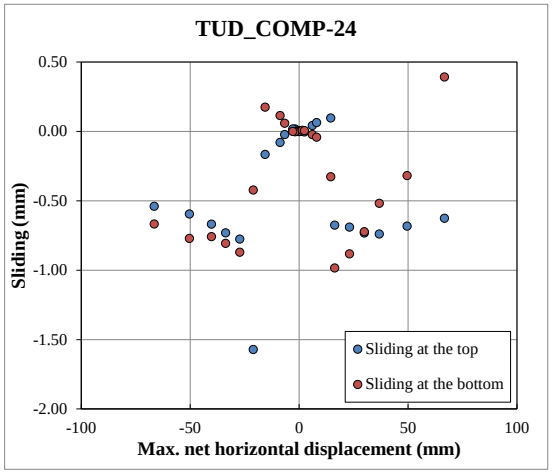

(b)

Figure 26 – Local deformation for wall TUD_COMP-24: (a) Crack opening and crushing; (b) Sliding.

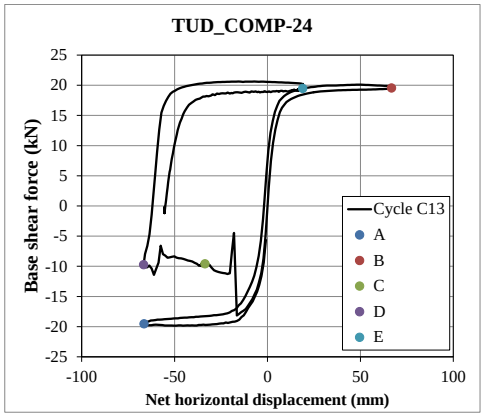

(a)

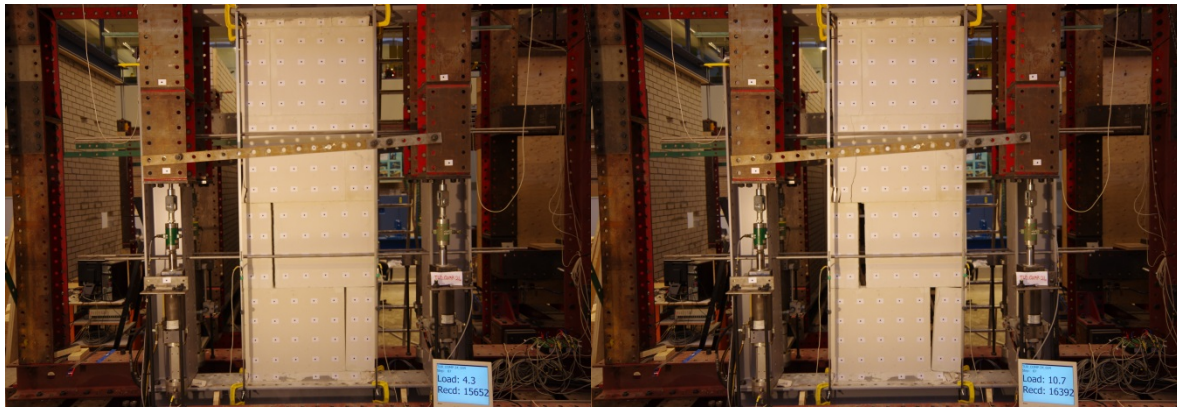

(b) Point A – u = -66.4 mm, F = -19.5 kN (c) Point B – u = +66.8 mm, F = +19.5 kN

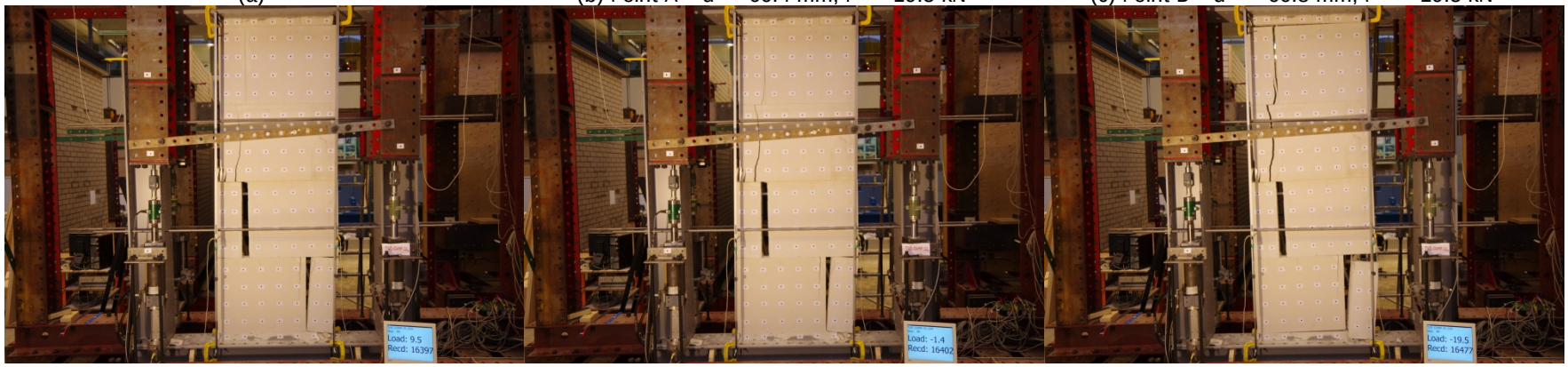

(d) Point C – u = -33.7 mm, F = -9.6 kN (e) Point D – u = -66.7 mm, F = -9.7 kN (f) Point E – u = +19.0 mm, F = +19.5 kN

Figure 27 – Crack pattern of wall TUD_COMP-24 during cycle C13: (a) Capacity curve; (b)-(f) Crack pattern at selected points.

6.3.2 Wall TUD_COMP-25

The wall TUD_COMP-25, made in calcium silicate element masonry, was tested under cantilever configuration with a pre-compression load of 0.60 MPa. The test was performed in 16 cycles. In the first cycle C0F, a force of 1.4 kN was applied and a jack's displacement of +/- 0.45 mm was measured. In the following three cycles (C1D, C2D and C3D) a jack's displacement equal to 1, 2 and 3 times the measured displacement was applied. Subsequently, increments in drift were applied. In Table 13 the complete loading history is reported in terms of net horizontal displacement and corresponding drift.

Table 13 – Loading history for wall TUD_COMP-25.

Cycle	Net displacement		Drift	
C1D	0.00	0.05	0.00	0.00
C2D	-0.02	0.10	0.00	0.01
C3D	-0.15	0.11	-0.01	0.01
C1	-0.20	0.11	-0.01	0.01
C2	-1.41	1.09	-0.05	0.04
C3	-2.59	2.27	-0.09	0.09
C4	-3.79	3.46	-0.14	0.13
C5	-8.70	8.24	-0.32	0.30
C6	-18.50	18.09	-0.68	0.66
C7	-28.29	27.96	-1.04	1.03
C8	-38.04	37.71	-1.40	1.38
C9	-49.65	45.40	-1.82	1.67
C10	-59.58	54.43	-2.18	2.00
C11	-71.89	68.74	-2.63	2.52
C12	-84.28	85.29	-3.06	3.12

Figure 28 shows the in-plane behaviour of wall TUD_COMP-25 in terms of capacity curve and drift, while Figure 29 shows the relation between the net vertical and net horizontal displacement. The initial stiffness of the wall was estimated in cycle C2D and it is equal to K = 6 kN/mm. The wall TUD_COMP-25 shows a maximum base shear force of +10.50 and -10.22 kN in the positive and negative loading direction, respectively. In the post-peak phase, no degradation in force could be observed that did not result in a change of energy dissipation mechanism (Figure 30). After achieving the maximum base shear force, an out-of-plane rotation of the wall occurred; this resulted in a misaligned between the wall and the kicker layer. The test was carried out up to a maximum displacement of -84.28/+85.29 mm corresponding to a drift of -3.06/+3.12 % was applied. Although no reduction in base shear force was achieved, the test was stopped because large in-plane deformation were reached and because out-of-plane deformations of the wall started to develop (Figure 31c).

The wall showed a pure rocking mechanisms. In cycle C2 (d_r = 0.05 %), a first crack occurred between the bottom kicker layer and the first course of masonry. This crack could reach a maximum opening of approximatively 25 mm as shown in Figure 31a. The sliding at this interface was limited (Figure 31b). Due to the high slenderness ratio of the wall and the pure rocking mechanism, out-of-plane deformation of the wall occurred allowing a misaligned between the wall and the kicker layer (Figure 32). The cracking and crushing of the bottom kicker (Figure 32) layer started during cycle 10 (d_r = 2.1 %).

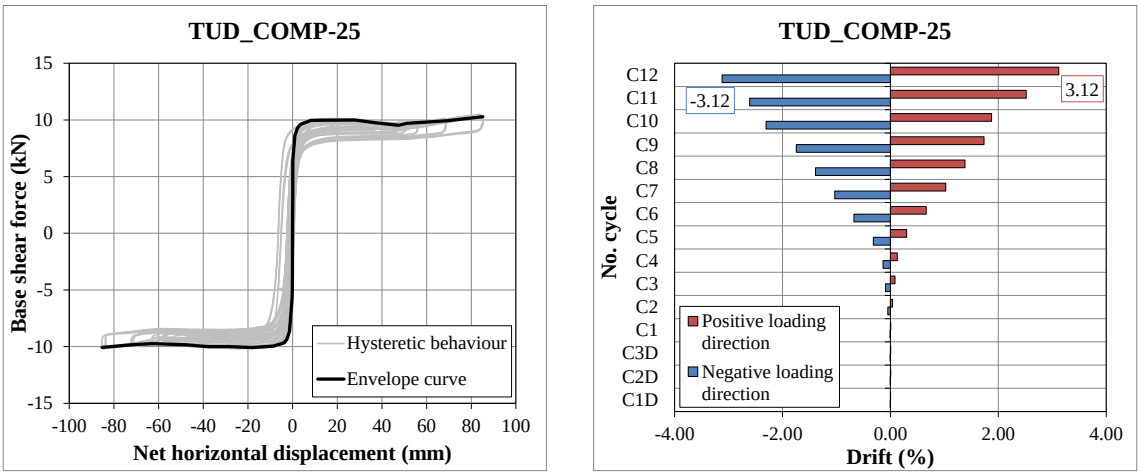

(a) (b)

Figure 28 – In-plane behaviour of wall TUD_COMP-25: (a) Capacity curve; (b) Drift.

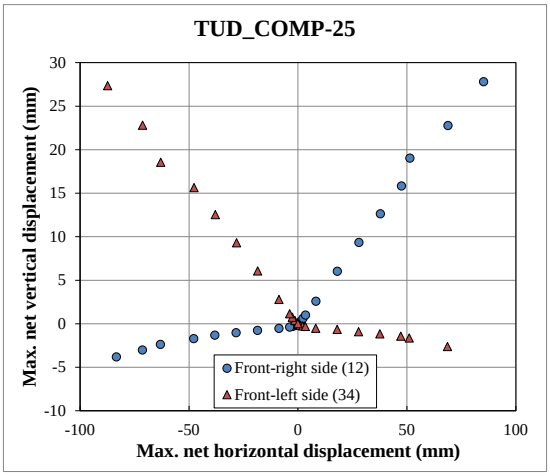

Figure 29 – Vertical versus horizontal displacement for wall TUD_COMP-25.

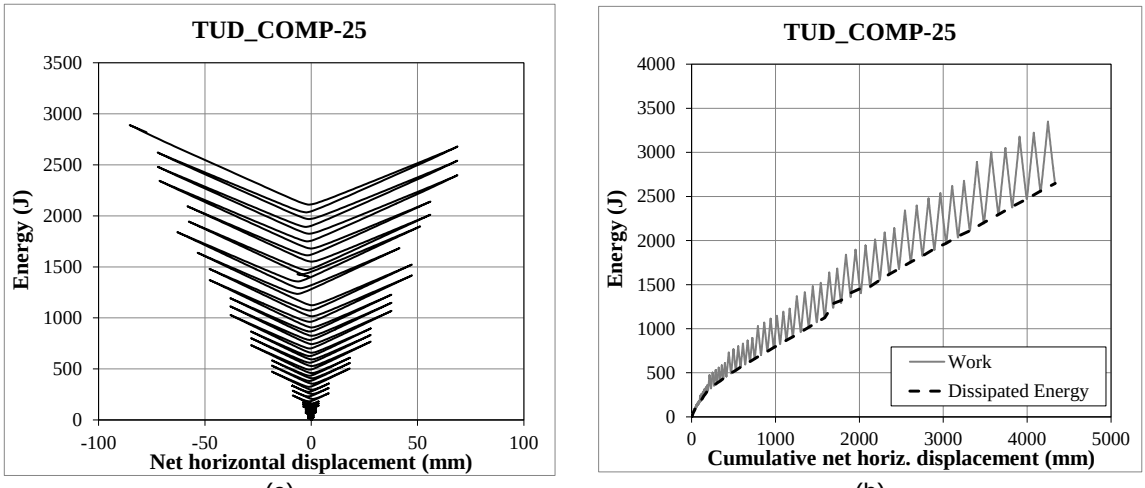

(a) (b)

Figure 30 – Energy dissipation for wall TUD_COMP-25: (a) Energy vs. net horizontal displacement; (b) Work and dissipated energy vs. cumulative net horizontal displacement.

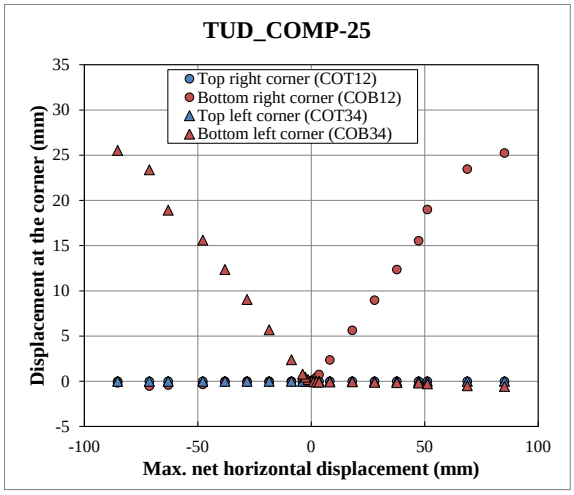

(a)

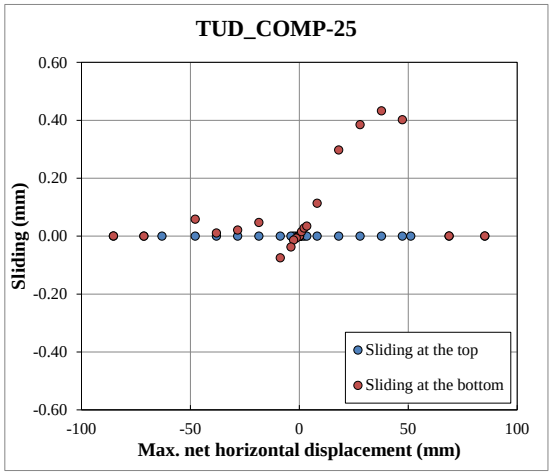

(b)

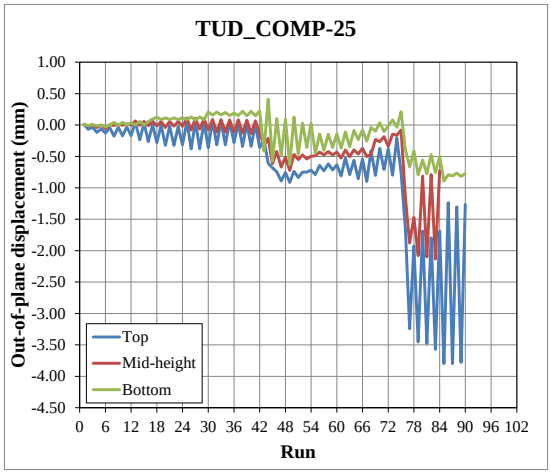

(c)

Figure 31 – Local deformation for wall TUD_COMP-25: (a) Crack opening and crushing; (b) Sliding; (c) Out-of-plane deformations.

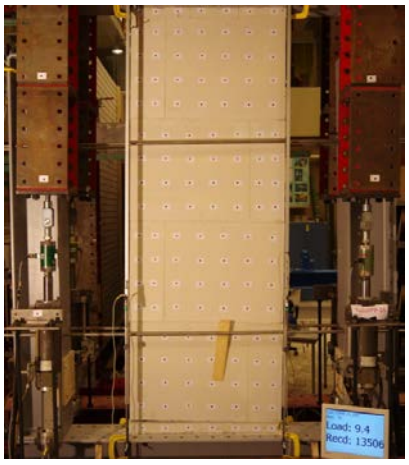

(a)

(b)

Figure 32 – Crack pattern of wall TUD_COMP-25 at the end of the test: (a) Overview; (b) Detail bottom-right corner.

7 Comparison per masonry type

In order to compare the in-plane behaviour of the different masonry walls, the equivalent bilinear approximation is adopted [10]. The equivalent bilinear curve can be created on the basis of the envelope curve that is defined as: "the locus of extremities of the load-displacement hysteresis loops, which contains the peak loads from the first" run "of each phase of the cyclic loading and neglects points on the hysteresis loops where the absolute value of the displacement at the peak load is less than that in the previous phase" [11]. The equivalent bilinear curve (Figure 33) can be expressed as follows:

$$V = \begin{cases} K_{el}u & u < u_{el} \\ V_u & u_{el} \le u \le u_u \end{cases} \tag{4}$$

where K_{el} is the stiffness determined from the envelop curve as the secant stiffness corresponding to a stress level equal to 0.7 time the maximum base shear force, u_u is the ultimate displacement determined from the envelope curve at a residual capacity equal to 80% of the maximum base shear force, V_u is the maximum base shear force of the bilinear curve determined by imposing that the area underneath the bilinear and the envelop curve up to the displacement u_u are the same and u_{el} is the elastic displacement determined as $u_{el} = V_u/K_{el}$.

In order to determine the ductility of the wall, the ductility factor is defined as:

$$\mu_b = \frac{u_u}{u_{el}} \tag{5}$$

By adopting the equivalent bilinear curve the displacement at ultimate limit state is defined in correspondence of a residual base shear capacity equal to 80% of the maximum base shear force. By using the ultimate displacement u_u, the ultimate drift obtained from the equivalent bilinear curve $d_{r\text{-}b}$ can be estimated.

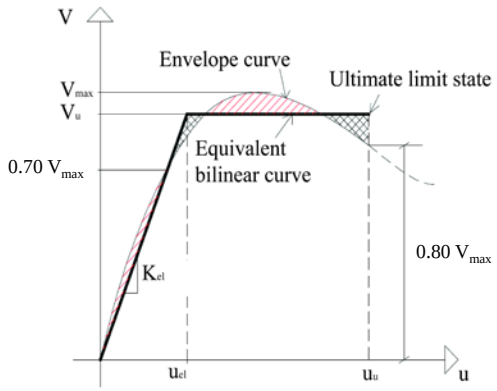

Figure 33 – Equivalent bilinear curve (adapted from [10]).

Table 14 lists the parameters for the bilinear approximation (Eq. (4)), while Figure 34 and Figure 35 show the envelope and bilinear curve for the tested walls.
The slender walls in calcium silicate masonry (TUD_COMP-20, -24, -25) showed a flexural type of failure followed in some cases by toe crushing. Experimentally all walls showed high displacement capacity (drift d_r in Table 14), but the CS element masonry walls show higher ductility (μ_b ~ 60-95) with respect to the wall made of CS brick masonry (μ_b ~ 36).
The squat walls in clay brick masonry (TUD_COMP-21, -22, -23) showed a shear type failure among which both diagonal shear failure and sliding failure occurred. The wall TUD_COMP-22, which failed due to bed joint sliding at the base followed by toe crushing, shows the highest ductility (μ_b ~ 150). This high ductility value was reached thanks to the squat dimension of the wall which promotes the sliding mechanism prior to the rocking mechanism.
Generally, the ultimate drift identified with the bilinear approximation (d_{r-b} in Table 14) results maximum 30% lower than the one obtained experimentally, with the exception of wall TUD_COMP-21. This wall shows a brittle diagonal shear failure leading to a large degradation of base shear force in the post-peak phase.

Table 14 – Parameters for the bilinear approximation of the capacity curve.

Parameter and unit		**Specimen's name (TUD_COMP-)**											
		20		**21**		**22**		**23**		**24**		**25**	
		Neg.	**Pos.**	**Neg.**	**Pos.**	**Neg.**	**Pos.**	**Neg.**	**Pos.**	**Neg.**	**Pos.**	**Neg.**	**Pos.**
K_{el}	kN/mm	6.9	9.9	256.6	238.1	304.0	386.5	46.8	74.4	27.8	33.6	6.3	8.1
u_u	mm	-68.4	56.9	-4.2	3.8	-50.1	48.0	-47.0	49.9	-66.4	66.8	-85.3	85.2
V_u	kN	-13.6	13.8	-88.4	88.8	-114.3	111.4	-99.7	79.6	-20.4	20.5	-9.9	9.9
u_{el}	mm	-2.0	1.4	-0.3	0.4	-0.4	0.3	-2.1	1.1	-0.7	0.6	-1.6	1.2
μ_b	-	34.5	40.8	12.2	10.2	133.4	166.5	22.1	46.6	90.8	109.7	54.0	69.4
d_{r-b}	%	-2.46	2.05	-0.16	0.14	-1.86	1.78	-1.74	1.85	-2.45	2.46	-3.14	3.14
Failure mode		Rocking and toe crushing		Diagonal shear failure		Sliding and toe crushing		Diagonal shear failure		Rocking and splitting of the bottom unit		Rocking	

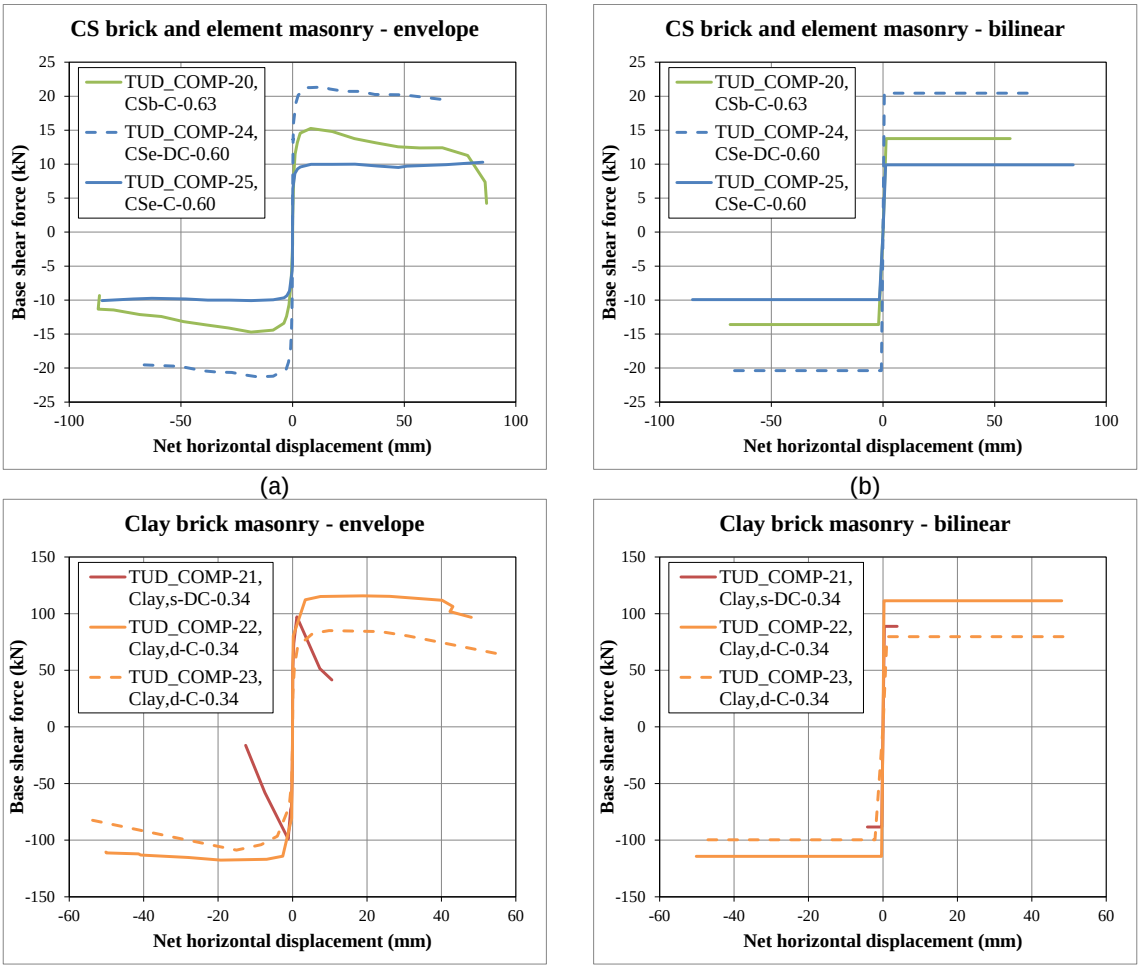

Figure 34 – Envelope and bilinear curves for: (a)-(b) CS brick and element masonry wall; (c)-(d) Clay brick masonry walls. In the legend the name of the wall is followed by the type of masonry, the type of boundary and the pre-compression stress in MPa (CSb = CS brick masonry, CSe = CS element masonry, Clay,s = Single wythe clay masonry, Clay,d = Double wythe clay masonry, C = Cantilever configuration, DC= double clamped configuration).

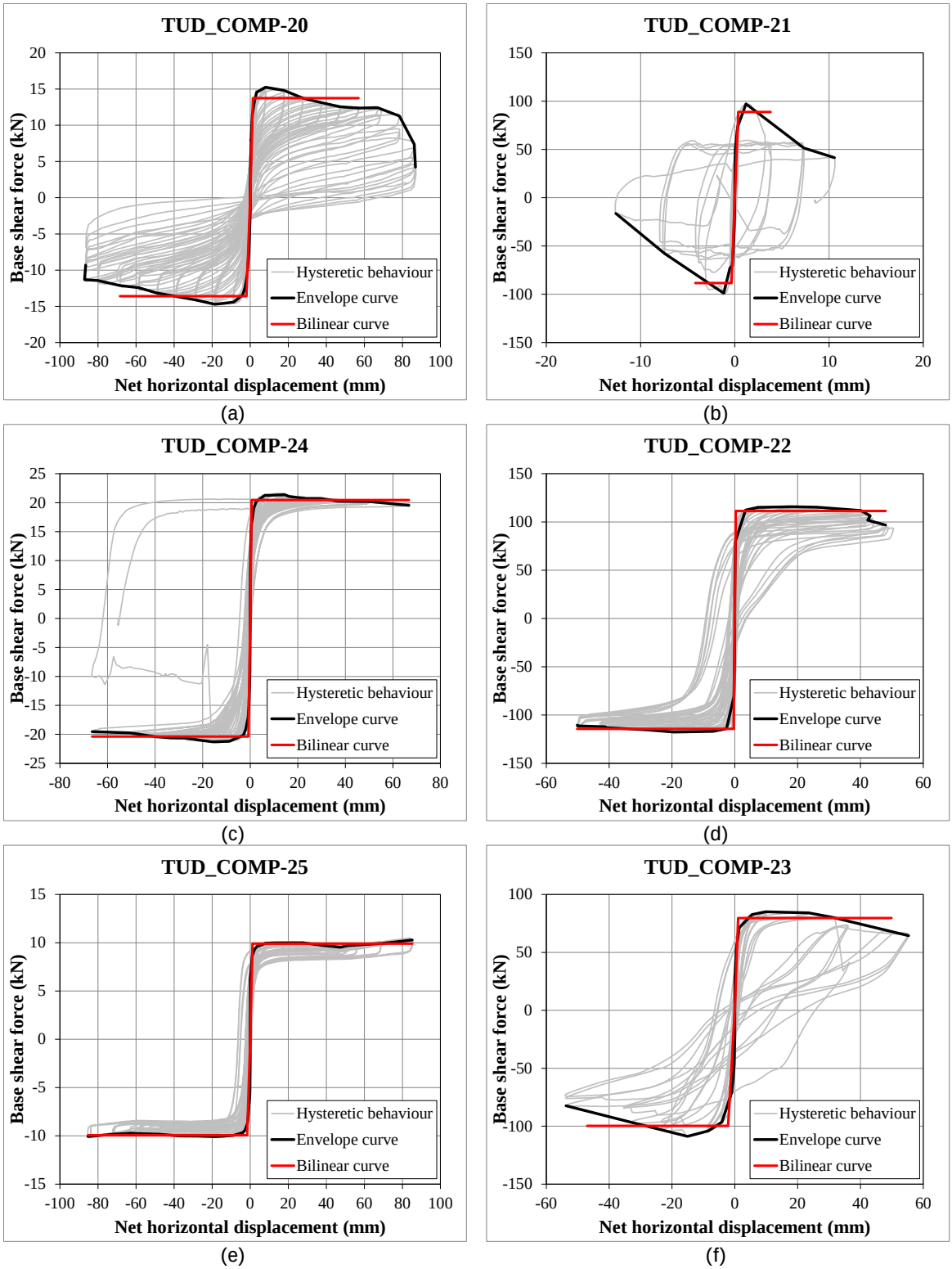

Figure 35 – Bilinear curves for: (a)-(c)-(e) CS brick and element masonry wall; (b)-(d)-(f) Clay brick masonry walls.

8 Analytical calculations

In this Section the analytical formulation for the estimation of the maximum base shear force (Section 8.1) and the ultimate drift (Section 8.2) are reported. A comparison with the experimental results is presented (Section 8.3).

8.1 Maximum base shear force

The resistance of masonry wall subject to in-plane loading can be estimated in agreement with Eurocode 8 [3] and NPR 9998 [4] for the assessment of existing masonry buildings. Both methods distinguish between flexural or shear type failure modes.

In order to compare the experimental and numerical results modifications should be applied to the analytical formulation to consider features related to the adopted test set-up (Section 5.1 and Figure 36).
To estimate the maximum base shear force of unreinforced masonry wall as controlled by flexural failure, the following corrections should be applied:

- the effective height calculated as $H_{eff} = H_w - 2h_u$ should be considered. This accounts for the fact that the first and last course of masonry are glued on the bottom and top steel beam, thus rocking of the pier can occur only between the first and last mortar bed joint.
- a correction factor equal to $H_{eff}/(H_{eff} + H_a)$ should be applied to the analytical estimation of the base shear force. This factor accounts for the fact that the horizontal load is applied at a distance H_a from the top of the wall. This distance is equal to the height of the last course of masonry (glue on the top beam) and half of the height of the top beam (300 mm).

To estimate the maximum base shear force of unreinforced masonry wall as controlled by shear failure , no correction factors should be applied.
Furthermore, the mean values of the material properties (Section 4) are adopted in the analytical calculations.

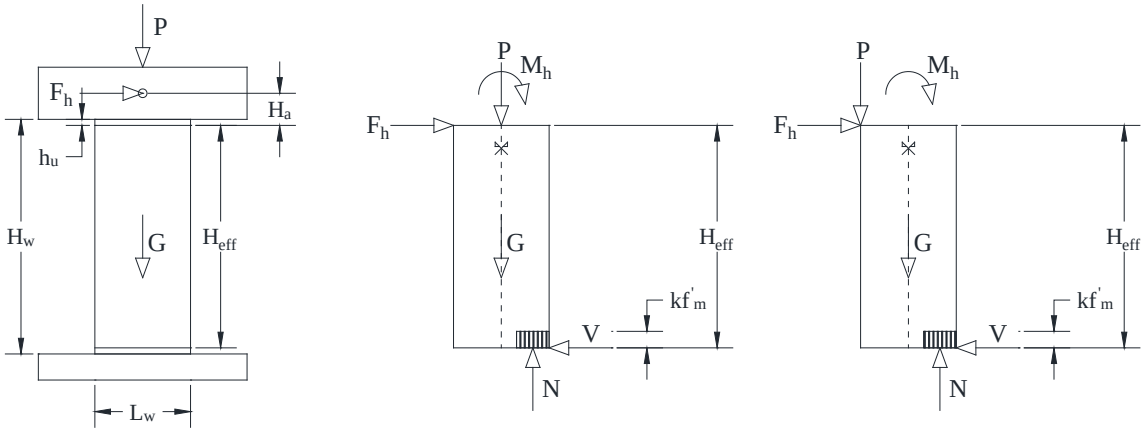

(a) (b) (c)

Figure 36 – Static scheme for wall subjected to in-plane action: (a) Geometry an loading conditions of the wall in the test set-up; (b) Static scheme for cantilever configuration; (c) Static scheme for double clamped configuration.

In **Eurocode 8** [3], the shear capacity of an unreinforced masonry wall can be controlled by either flexural or shear failure.
The base shear force capacity of an unreinforced masonry wall as controlled by **flexural failure** can calculated with equation (C.1) of section 4.2.1(3) in Eurocode 8. By applying the aforementioned modifications, it results:

$$V_f = \frac{L_w P}{2H_0}\left(1-1.15\frac{P}{L_w t_w f_m^{'}}\right)\frac{H_{eff}}{H_{eff}+H_a} \tag{6}$$

where P is the overburden load applied at the top of the wall, L_w is the in-plane horizontal dimension of the wall (length) and t_w is the thickness of the wall, H_0 is the distance between the section where the flexural capacity is attained and the contra-flexural point ($H_0=H_{eff}$ for cantilever configuration, and $H_0=0.5H_{eff}$ for double clamped configuration). It should be noted that in Eq. (6), the effect of the self-weight of the masonry wall is not included.
The shear force capacity of an unreinforced masonry wall controlled by **shear failure**, may be taken according to equation (C.2) of section 4.3.1(3) in Eurocode 8:

$$V_{sh} = f_{vd} L_w^{'} t_w \tag{7}$$

where L_w' is the length of the compressed area of the wall, t_w is the thickness of the wall and f_{vd} is the masonry mean shear strength accounting for the presence of vertical load. Similarly to the formulation suggested in the code, f_{vd} is evaluated according to a frictional law (based on a Coulomb friction criterion, which can be physically justified especially in the cases where diagonal cracking is associated with mortar bed- and head-joint failure), according to the following equation:

$$f_{vd} = f_{v0} + \mu\sigma_v \tag{8}$$

with f_{v0} the initial shear strength of the material (i.e. the mean shear strength in absence of vertical load), μ the friction coefficient (whereas in equation (C.2) μ is substituted by the constant value 0.4) and $\sigma_v=P/(L_w t_w)$ is the applied vertical pressure.
However, the equation reported in the code does not provide a direct evaluation of L_w'. An explicit prediction of the shear strength, where a calculation of the compressed length of the wall L_w' is included, is provided in [12], and can be computed according to the following equation:

$$V_{sh} = L_w t_w \frac{1.5 f_{v0} + \mu\sigma_v}{1+3\frac{H_0}{L_w}\frac{f_{v0}}{\sigma_v}} \tag{9}$$

The base shear capacity of an unreinforced masonry wall is evaluated as the smallest between the values given by Eqs. (6) and (9):

$$V_{EC8} = \min\left(V_f, V_{sh}\right) \tag{10}$$

In **NPR 9998** [4] the shear capacity of an unreinforced masonry wall can be governed by diagonal tension failure, premature toe crushing, rocking and bed joint-sliding. The case of slip plane sliding on damped-proof membrane it is not considered here because it does not apply.
The base shear force capacity of an unreinforced masonry wall as controlled by **diagonal tensile failure** can calculated with equation (G.31) of section G.9.2.1 in NPR 9998:

$$V_{dt} = f_{dt} L_w t_w \beta \sqrt{1+\frac{f_a}{f_{dt}}} \tag{11}$$

where L_w is the in-plane horizontal dimension of the wall (length) and t_w is the thickness of the wall, β is a coefficient depending on the slenderness of the wall, f_a is the axial compression stress due to gravity loads calculated at mid-height of the wall (thus including the self-weight of the masonry wall) and f_{dt} is the diagonal tensile strength.

The coefficient β is estimated as:

$$\beta = \begin{cases} 1.00 & H_w/L_w < 0.5 \\ 1 - 0.33 H_w/L_w & 0.5 < H_w/L_w < 1.5 \\ 0.67 & H_w/L_w > 1.5 \end{cases} \quad (12)$$

The diagonal tensile strength f_{dt} is estimated as:

$$f_{dt} = 0.5 f_{v0} + \mu f_a \quad (13)$$

with f_{v0} the initial shear strength and μ the coefficient of friction.
The base shear force capacity of an unreinforced masonry wall as controlled by **premature toe crushing** can be calculated with equation (G.33) of section G.9.2.2 in NPR 9998. By applying the aforementioned corrections to account for the adopted set-up, it results:

$$V_{tc} = \left(\alpha P + \frac{G}{2} \right) \frac{L_w}{H_{eff}} \left(1 - \frac{f_a}{0.7 f_m^{'}} \right) \frac{H_{eff}}{H_{eff} + H_a} \quad (14)$$

where P is the overburden load applied at the top of the wall, G is the self-weight of the masonry wall, f_a is the axial compression stress due to gravity loads calculated at mid-height of the wall, f'_m is the mean compressive strength of masonry, α is a constant equal to 0.5 for cantilever configuration and 1 for double clamped configuration, L_w is the in-plane horizontal dimension of the wall (length) and H_{eff} is the effective height as defined in Figure 36, H_a is the distance between the point of application of the horizontal load and the top of the wall.
The formulation of NPR 9998 for premature toe crushing (Eq. (14)) can be compared with the one for flexural failure presented by Eurocode 8 (Eq. (6)). The following differences can be found:

- the formulation proposed by the NPR 9998 accounts for the contribution of half of the self-weight of the masonry wall, which is neglected in Eurocode 8. However, in the formulation proposed by the NPR 9998, the coefficient α that accounts for the different boundary conditions is applied only to the overburden and not on the self-weight.
- the formulation proposed by the NPR 9998 considers that the maximum stress at the toe is equal to 0.7 times the compressive strength of the masonry f'_m, while in Eurocode 8 a factor 0.87 is considered.

The base shear force capacity of an unreinforced masonry wall as controlled by **rocking** can be calculated with equation (G.36) of section G.9.2.3 in NPR 9998. By applying the aforementioned corrections to account for the adopted set-up, it results:

$$V_r = 0.9 \left(\alpha P + \frac{G}{2} \right) \frac{L_w}{H_{eff}} \frac{H_{eff}}{H_{eff} + H_a} \quad (15)$$

By comparing the formulation for premature toe crushing (Eq. (14)) and rocking (Eq. (15)) proposed by NPR 9998 the following observation can be made:

- failure governed by rocking can govern with respect to the failure governed by premature toe crushing only if the axial compression stress due to gravity loads calculated at mid-height of the wall f_a is lower than 0.07 time the mean compressive strength of masonry f'_m ($f_a < 0.07\, f'_m$).
- in the formulation for rocking failure no direct link is made with the compressive strength of the masonry (as done in Eurocode 8) to consider toe crushing after pure rocking; the reduction factor 0.9 is considered.

The base shear force capacity of an unreinforced masonry wall as controlled by **bed joint sliding** can be calculated with equation (G.38) of section G.9.2.4 in NPR 9998:

$$V_s = 0.7 \left(t_w L_w f_{v0} + \mu \left(P + G \right) \right) \quad (16)$$

where G is the self-weight of the masonry wall above the sliding plane.

The formulation of NPR 9998 for bed joint sliding (Eq. (16)) can be compared with the one for shear failure presented by Eurocode 8 (Eq.(7)). The following differences can be found:

- Eurocode 8 estimates the shear resistance by considering the length of the compressed area of the wall L'_w, for which however a formulation is not provided. On the contrary, the NPR 9998 calculates the bed joint sliding strength on the un-cracked section length L_w and applies a reduction coefficient equal to 0.7.
- the formulation proposed by the NPR 9998 accounts for the contribution of the self-weight of the masonry wall above the sliding plane, which is neglected in Eurocode 8

The base shear capacity of an unreinforced masonry wall is evaluated as the smallest between the values given by Eqs. (11), (14), (15) and (16):

$$V_{NPR} = \min\left(V_{dt}, V_{tc}, V_r, V_s\right) \tag{17}$$

8.2 Ultimate drift

The displacement capacity of the wall can be expressed in term of ultimate *drift* d_r, defined as the ratio between horizontal displacement u and the height of the wall H_w.

Following **Eurocode 8** [3], the drift at near collapse state for masonry wall subject to **flexural failure** can be calculated in agreement with section C.4.2.2(2):

$$d_{r-f} = \frac{4}{3} 0.008 \frac{H_0}{L_w} \tag{18}$$

while for masonry wall subject to **shear failure** is assumed equal to $d_{r\text{-}sh} = 0.5\%$ in agreement with section C.4.3.3(2).

In **NPR 9998** [4], the **diagonal tensile failure** and the **premature toe crushing** are considered both brittle failure mechanisms. Considering that these mechanisms are undesired, the drift at near collapse should not be higher than the one corresponding to the yield displacement u_y. The yield displacement u_y can be estimated with an elastic formulation considering a reduced stiffness representative of the cracked wall. In this case a reduction of 50% of the initial stiffness is considered.
Following NPR 9998, the drift limits for **rocking failure** can be calculated with Eq. G.37 in section G.9.2.3:

$$d_{r-r} = 0.01\left(1 - 2.2\frac{f_a}{f'_m}\right)\sqrt[3]{\frac{H_w}{L_w}} \tag{19}$$

where fa is the axial compression stress due to gravity loads at the base of the pier.
Following NPR 9998, the drift limits for **bed joint sliding failure** is taken equal to $d_{r\text{-}s}$ = 0.75% in agreement with G.9.2.4(6).

The drift limits proposed in the NPR 9998 for rocking failure were derived by a statistical study performed at **TU Delft** [13] on the capacity of rocking walls. The study analysed several in-plane tests on walls available in literature including also the wall TUD_COMP-20, -24 and -25 presented in this report. Following the TU Delft study, the drift can be calculated as:

$$d_{r-TUD} = 0.0018 \cdot \left(1 - 2.2\frac{\sigma_v}{f'_m}\right) \cdot \sqrt[3]{\frac{H_w}{L_w}} \tag{20}$$

It should be noted that the drift limit presented in Eq. (19) has been evaluated as the 5%-percentile of the sample distribution, which was considered for the estimation of Eq. (20).

8.3 Comparison with experimental results

In this Section the estimation provided by the analytical formulations are compared with the experimental results in terms of maximum base shear force and ultimate drift.

Table 15 lists the parameters used for the analytical calculation.

Table 15 – Analytical estimations of the force and displacement capacity for the tested specimens.

Parameters	Symbol	Unit	Specimen's name (TUD_COMP-)				
			20	21	22	24	25
Masonry type	-	-	CS brick	Clay single wythe	Clay double wythe	CS element	CS element
Slenderness ratio	H_w / L_w		2.50	0.86	0.90	2.77	2.77
Height wall	H_w	mm	2780	2695	2700	2715	2715
Length wall	L_w	mm	1110	3140	2995	979	979
Thickness wall	t_w	mm	101	102	210	100	100
Height glued unit	h_u	mm	71	50	50	70	70
Effective height	H_{eff}	mm	2638	2595	2600	2575	2575
Distance for eccentricity of the load	H_a	mm	371	350	350	370	370
Correction factor	$H_{eff}/(H_{eff}+H_a)$	-	0.88	0.88	0.88	0.87	0.87
Weight of the top steel system	W_t	kN	29.50	38.00	38.00	29.50	29.50
Applied load in vertical actuators	F_L+F_R	kN	40.60	70.00	176.0	29.00	29.00
Self-weight masonry	G	kN	5.63	14.74	29.01	4.85	4.85
Overburden stress	σ_v	Mpa	0.63	0.34	0.34	0.60	0.60
Axial stress at mid-height	$\sigma_{a\text{-}mid}$	Mpa	0.65	0.36	0.36	0.62	0.62
Density	ρ	kg/m^3	1805	1708	1708	1824	1824
Compressive strength	f'_m	MPa	6.35	14.04	14.04	12.69	12.69
Initial shear strength	f_{v0}	MPa	0.13	0.18	0.18	0.83	0.83
Coefficient of friction	μ	-	0.5	0.69	0.69	1.48	1.48
Diagonal tensile strength	f_{dt}		0.39	0.35	0.35	1.34	1.34
Coefficient for boundary conditions	$\psi = H_0/H$	-	1	0.5	1	0.5	1
Coefficient for boundary conditions	α	-	0.5	1	0.5	1	0.5
Coefficient for nonlinear stress distribution	β	-	0.67	0.71	0.70	0.67	0.67

In Table 16 and Figure 37 the experimental and analytical results are compared in terms of maximum base shear force. The analytical formulation proposed by the Eurocode 8 and the NPR 9998 underestimates the base shear capacity with a maximum error of 16 and 22% respectively.
Some differences are noted in terms of failure mode estimation between the two codes. In this respect Figure 38 shows all the estimates provided by the Eurocode 8 (blue bars) and by the NPR 9998 (orange bars); in both groups the minimum value will determine the failure mechanism.
For the walls showing a flexural type failure (TUD_COMP-20, -24, -25), the estimate for flexural failure in Eurocode 8 and the estimations given by premature toe crushing and rocking in NPR 9998 give similar value. However, in the case of wall TUD_COMP-20 the formulation proposed by NPR 9998 predicts a premature toe-crushing failure rather than rocking failure. If this estimate is still accurate for the base shear

force capacity, it results in a limitation for the estimation of the displacement capacity as explained in next paragraph.
For the wall TUD_COMP-21 showing a shear type failure, similar predictions are provided by the two methods resulting in shear failure for the Eurocode 8 and bed joint-sliding failure for NPR 9998. It should be pointed out that in NPR 9998 distinguish between bed-joint siding failure and diagonal tensile failure, considering the latter as a brittle behaviour. Considering this definition, the behaviour of wall TUD_COMP-21 is closer to diagonal tensile failure rather than bed joint sliding.
For the wall TUD_COMP-22, showing an hybrid failure in sliding and toe crushing, both the Eurocode 8 and the NPR 9998 predict a rocking failure. Furthermore, by comparing the estimation for shear sliding given by the Eurocode 8 (V_{sh} =133.1 kN) with the estimation for bed joint sliding given by NPR 9998 (V_s = 191.5 kN) a difference of 30% is observed. This difference is not observed for the wall TUD_COMP-21.

Table 16 – Comparison between experimental and analytical results in terms of *base shear force*.

Specimen	Experimental results			Analytical calculations			
	V+	V-	Failure mode	V_{EC8}	Failure mode	V_{NPR}	Failure mode
	kN	kN		kN		kN	
TUD_COMP-20	-14.8	15.4	Rocking and toe crushing	12.9	Rocking	12.0	Premature toe-crushing
TUD_COMP-21	-98.9	97.2	Diagonal shear failure	98.3	Shear	97.0	Bed joint sliding
TUD_COMP-22	-117.8	116.7	Sliding and toe crushing	109.0	Rocking	111.2	Rocking
TUD_COMP-24	-21.5	21.6	Rocking and splitting of the bottom unit	19.4	Rocking	18.2	Rocking
TUD_COMP-25	-10.2	10.5	Pure Rocking (OOP deform)	9.7	Rocking	9.5	Rocking

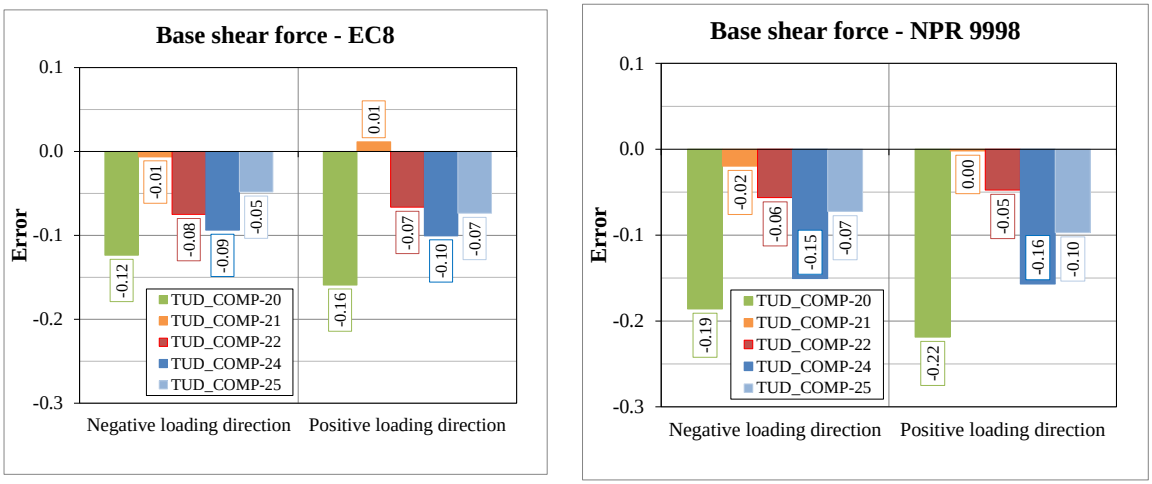

(a) (b)

Figure 37 – Error in the estimation of the base shear force capacity: (a) Eurocode 8; (b) NPR 9998.

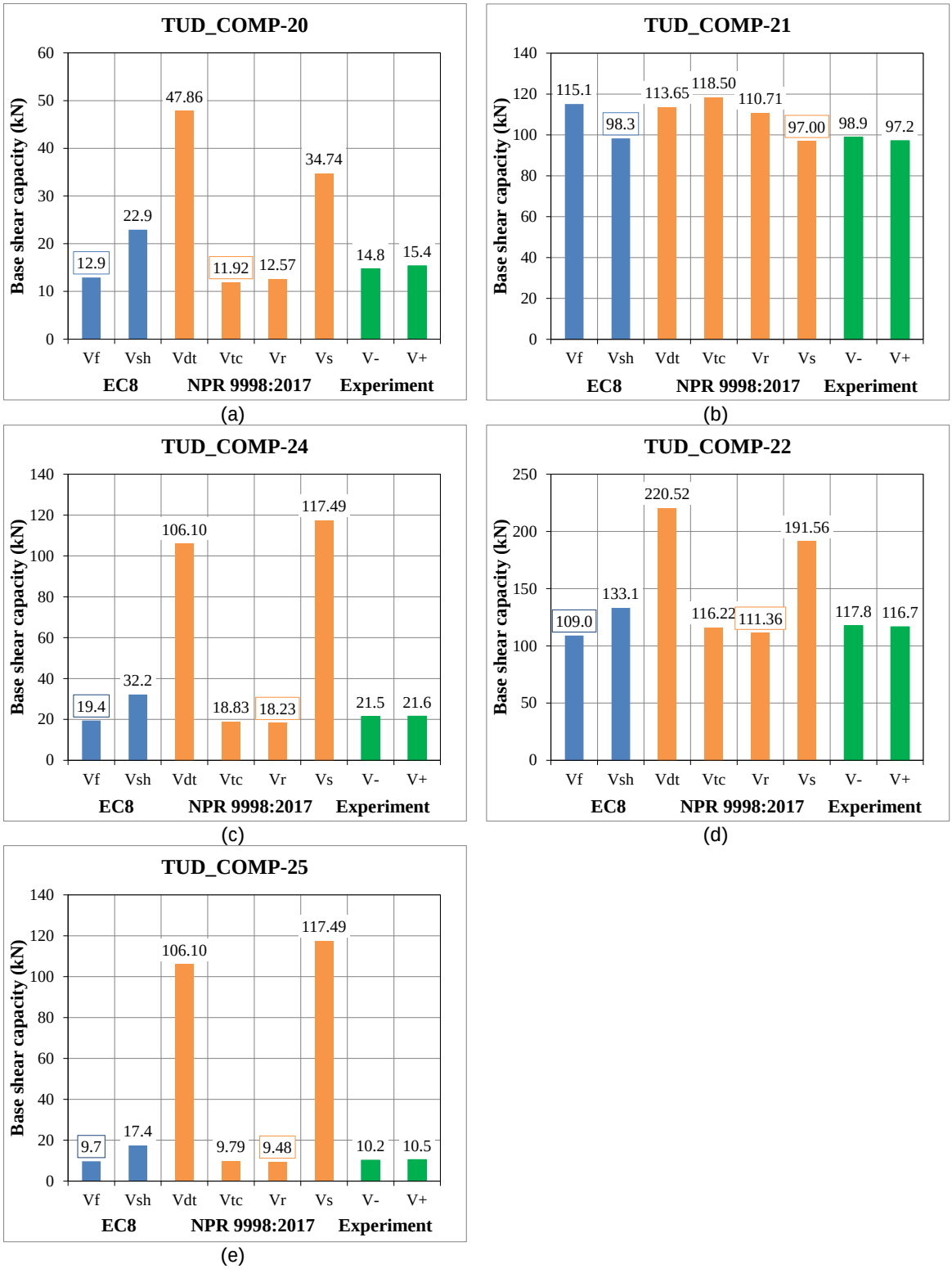

Figure 38 – Estimation of the base shear force capacity with Eurocode 8 (blue) and NPR 9998 (orange) in comparison with experimental results (green): (a)-(c)-(e) Flexural type failure; (b)-(d) Shear type failure.

In Table 17 and Figure 39 the experimental and analytical results are compared in terms of drift.
For the walls showing a flexural type failure (TUD_COMP-20, -24, -25), both methods provide a conservative estimate of the drift at near collapse with the NPR 9998 giving the most conservative value. For the wall TUD_COMP-20, which failed in rocking and subsequent toe crushing, the Eurocode 8 predicts a rocking failure with a 10% error in the drift estimation; on the contrary, the NPR 9998 predicts a premature toe crushing failure that results in un underestimation of 90% of the drift.
For the walls TUD_COMP-21 showing a shear type failure, both methods provide an overestimation of the drift with the NPR 9998 giving the largest error.
For the walls TUD_COMP-22 showing an hybrid failure mode, both methods provide an underestimation of the drift of approximatively 50%.

Table 17 – Comparison between experimental and analytical results in terms of *drift*.

Specimen	Experimental results			Analytical calculations				
	d_r^+	d_r^-	Failure mode	dr_{EC8}	Failure mode	dr_{NPR}	Failure mode	dr_{TUD}
	%	%		%		%		%
TUD_COMP-20	-3.13	3.13	Rocking and toe crushing	2.67	Rocking	0.17	Premature toe-crushing	1.91
TUD_COMP-21	-0.47	0.39	Diagonal shear failure	0.53	Shear	0.75	Bed joint sliding	
TUD_COMP-22	-1.86	1.78	Sliding and toe crushing	0.96	Rocking	0.87	Rocking	1.59
TUD_COMP-24	-2.45	2.46	Rocking and splitting of the bottom unit	1.48	Rocking	1.25	Rocking	2.27
TUD_COMP-25	-3.14	3.14	Pure rocking (OOP deform)	2.96	Rocking	1.25	Rocking	2.27

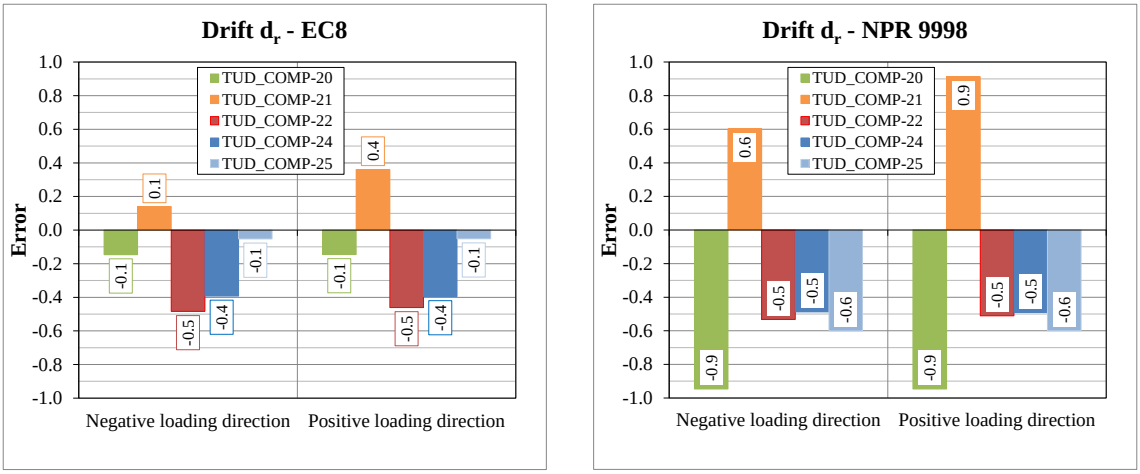

(a) (b)

Figure 39 – Error in the estimation of the ultimate drift d_r: (a) Eurocode 8; (b) NPR 9998.

Figure 40 shows the comparison between the experimental results and the analytical formulation proposed in Ref. [13]. The formulation (Eq. (20)) was based on experimental data and it estimates the ultimate drift with a coefficient of variation of approximatively 40%. It should be noted that the data analysis provided in Ref. [13] was based also on the experimental data for walls TUD_COMP-20, TUD_COMP-24 and TUD_COMP-25. Figure 40 confirms the 40% variation as reported in Ref. [13]. Furthermore, including in the comparison the wall TUD_COMP-22, which showed an hybrid failure composed by sliding at the base followed by toe crushing, the method provides a 10% error in the estimation of the ultimate drift.

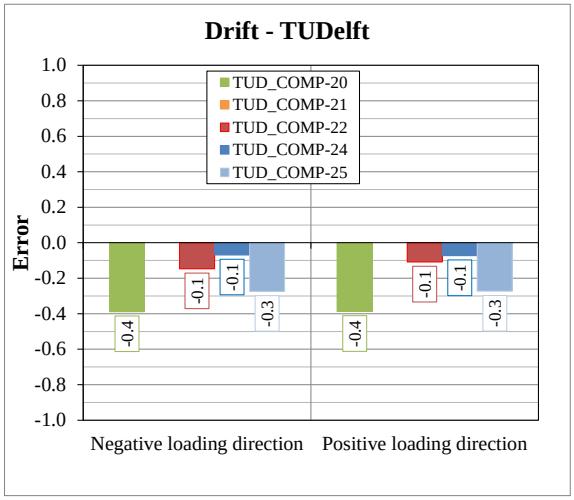

Figure 40 – Error in the estimation of the ultimate drift following the method proposed by in Ref. [13].

9 Summary and conclusions

Six in-plane shear-compression tests have been carried out at Stevin II laboratory of Delft University of Technology within the NAM Structural Upgrading project 2016/2017. Table 18 shows an overview of the results, while Figure 41 and Figure 42 show and overview of the failure mechanisms and the envelope curves, respectively.

Table 18 – Experimental results of the quasi-static in-plane tests performed in WP3.

Specimen	Unit type	L_w	H_w	t_w	σ_v	H_0/H	V^+	V^-	d_r^+	d_r^-	Failure mode
		mm	mm	mm	MPa	-	kN	kN	%	%	
TUD_COMP-20	CS brick	1110	2778	102	0.63	1	-14.8	15.4	-3.13	3.13	Rocking and toe crushing
TUD_COMP-21	Solid clay brick	3070	2710	100	0.36	0.5	-98.9	97.2	-0.47	0.39	Diagonal shear failure
TUD_COMP-22	Solid clay brick	2960	2710	210	0.36	1	-117.8	116.7	-1.86	1.78	Sliding and toe crushing
TUD_COMP-23	Solid clay brick	3070	2710	210	0.36	1	-108.9	85.4	-1.99	2.04	Rocking of 2 parts
TUD_COMP-24	CS elements	977	2743	100	0.6	0.5	-21.5	21.6	-2.45	2.46	Rocking and splitting of the bottom unit
TUD_COMP-25	CS elements	977	2743	100	0.6	1	-10.2	10.5	-3.14	3.14	Pure Rocking (OOP deform)

(a) TUD_COMP-20

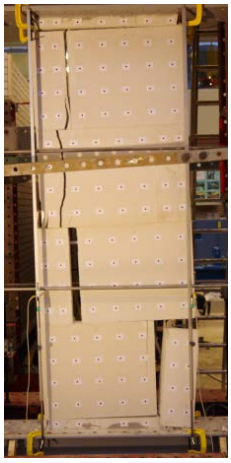

(b) TUD_COMP-24

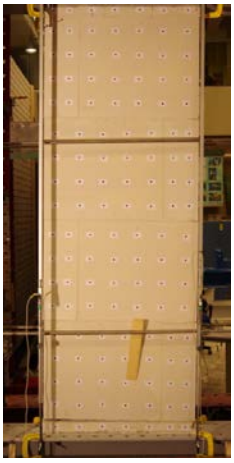

(c) TUD_COMP-25

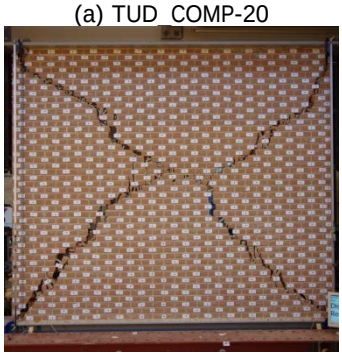

(d) TUD_COMP-21

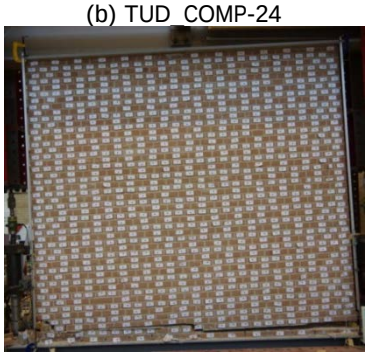

(e) TUD_COMP-22

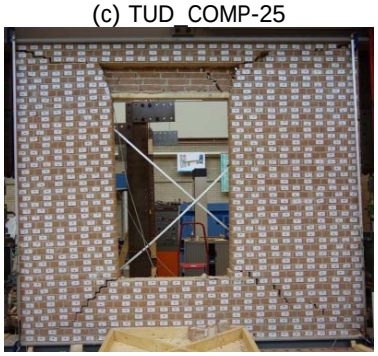

(f) TUD_COMP-23

Figure 41 – Overview of in-plane failure mechanisms for: (a)-(c) CS brick and element masonry walls; (d)-(f) clay brick masonry walls.

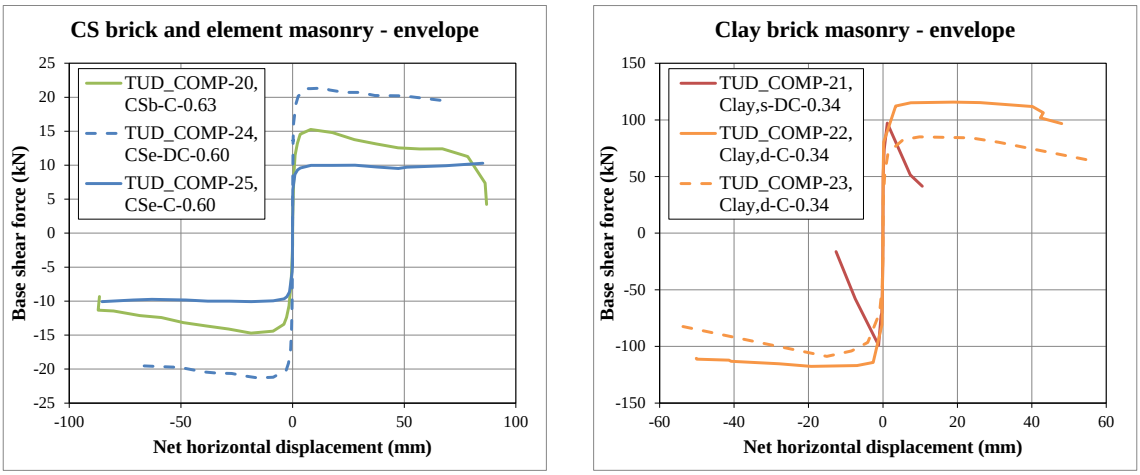

(a) (b)

Figure 42 – Envelope curves for: (a) CS brick and element masonry wall; (b) Clay brick masonry walls. In the legend the name of the wall is followed by the type of masonry, the type of boundary and the pre-compression stress in MPa (CSb = CS brick masonry, CSe = CS element masonry, Clay,s = Single wythe clay masonry, Clay,d = Double wythe clay masonry, C = Cantilever configuration, DC= double clamped configuration).

By observing the experimental results, the following conclusions can be drawn:

- The modification applied to the set-up lead to a successful results. In all tests large displacement could be achieved representative of the near collapse state.
- The slender walls in calcium silicate masonry (TUD_COMP-20, -24 and -25) showed a flexural type failure consisting in rocking failure followed by toe crushing. In the case of CS brick masonry wall the a gradual degradation of the base shear force is observed in the post-peak phase. On the contrary, in the case of the CS element masonry wall a large ductility in the post peak phase is observed followed by a rapid degradation in base shear force. This difference can be correlated to the brittle behaviour of the CS element masonry.
- The wall TUD_COMP-21 in single wythe clay brick masonry showed a brittle diagonal shear failure with a rapid degradation of the capacity in the post-peak phase. For this wall the lowest ductility factor is estimated (μ_b ~ 11).
- The squat wall TUD_COMP-22 in double wythe clay brick masonry showed an hybrid failure consisting of bed joint sliding at the bottom of the wall followed by toe crushing. For this wall the highest ductility factor is estimated (μ_b ~ 150).
- The wall with opening TUD_COMP-23 in double wythe clay brick masonry showed first the failure of the masonry lintel followed by the separation of the structure in two portions that were subject to rocking mechanism. This benchmark was adopted to study the diagonal tensile stepwise crack pattern in double wythe masonry. From the experiment, it is possible to note that the stepwise cracking uniformly develop within the thickness of the wall.

By comparing the experimental results with the analytical formulation proposed by Eurocode 8 and NPR 9998, the following observations can be made:

- it is possible to conclude that both methods estimate the maximum base shear force within a maximum error of 20%
- For the case of flexural type failure, the two methods provide similar results with the exceptions of wall TUD_COMP-20 (rocking followed by toe crushing) for which the NPR 9998 predicts a premature toe crushing failure leading to a large underestimation of the displacement capacity. In the NPR 9998 the premature toe crushing failure is distinguished from the rocking failure followed by toe crushing and it is considered as an undesired brittle failure mode. Consequently, a low ultimate drift is prescribed in this standard.
- For the case of the wall TUD_COMP-21 (diagonal shear failure), similar estimations of the maximum bases shear force are provided by the two methods; however overestimation of the ultimate drift are provided by both methods with the NPR 9998 giving the largest difference. The NPR9998, differently than the Eurocode 8, predicts a bed joint sliding failure rather than a diagonal tensile failure. Although both modes belong to the shear type failure, the formulation in the NPR

9998 aims to distinguish between the brittle diagonal tensile failure and the more ductile bed joint sliding failure. In this respect, although the wall TUD_COMP-21 showed a stepwise crack similarly to the one generally observed for bed joint sliding failure, the failure type can be classified as brittle thus more similar to the diagonal tensile failure defined by the NPR 9998.

- For the case of wall TUD_COMP-22 showing a hybrid failure, composed by bed joint sliding (on a single plane) followed by toe crushing, both methods predicts a rocking type failure. In this respect, the estimation of both the maximum base shear force and the ultimate drift are accurate.
- It should be pointed out that the observations drawn in this report on the comparison between experimental and analytical results are based on a limited number of data.

10 Reference

[1] Esposito, R., Rots, J.G., Ravenshorst, G., van Beek, T. (2016). Structural upgrading of masonry structures in the Groningen Area. Proposed TU DELFT testing program 2016. Delft University of Technology. Version 6, 22 March 2016.

[2] Esposito, R. and Ravenshorst, G. Quasi-static cyclic tests on masonry components. Plan of approach and testing protocol. Delft University of Technology. Report No. C31B67WP3-3, Final version 13 December 2016.

[3] EN 1998-3+C1 (2013). Eurocode 8 – Design of structures for earthquake resistance - Part 3: Assessment and retrofitting of buildings. Nederlands Normalisatie-instituit (NEN).

[4] NEN NPR 9998. Assessment of structural safety of buildings in case of erection, reconstruction and disapproval - Basic rules for seismic actions: induced earthquakes. Nederlands Normalisatie-instituit (NEN). 21 June 2017.

[5] Ravenshorst, G. and Messali, F., (2016): In-plane tests on replicated masonry walls. Delft University of Technology. Version 6, Final report 27 May 2016.

[6] Graziotti, F., Tomassetti, U., Rossi, A., Marchesi, B., Kallioras, S., Mandirola, M, Fragomeli, A., Mellia, E., Peloso, S., Cuppari, F., Guerrini, G., Penna, A., Magenes, G. (2016). Experimental campaign on a clay URM full-scale specimen representative of the Groningen building stock. Report EUC128/2016U, Eucentre, Pavia, IT. Version 20 July 2016

[7] Jafari, S. Esposito, R. (2016). Material tests for the characterisation of replicated calcium silicate brick masonry. Delft University of Technology. Report No. C31B67WP1-9, Final version, 14 November 2016.

[8] Jafari, S. Esposito, R. (2017). Material tests for the characterisation of replicated solid clay brick masonry. Delft University of Technology. Report number C31B67WP1-12, in preparation.

[9] Jafari, S. Esposito, R. (2017). Material tests for the characterisation of replicated calcium silicate element masonry. Delft University of Technology. Report number C31B67WP1-11, in preparation.

[10] Magenes, G., Morandi, P. and Penna, A. (2008). In-plane cyclic tests of calcium silicate masonry walls. Proceedings of 12th International Brick/Block Masonry Conference, 18-20 February, Sydney Australia.

[11] ASTM E2126-11 (2011). Standard Test Methods for Cyclic (Reversed) Load Test for Shear Resistance of Vertical Elements of the Lateral Force Resisting Systems for Buildings. ASTM International.

[12] Magenes, G., and Calvi, G. M., (1997). In-plane seismic response of brick masonry walls. Earthquake engineering & structural dynamics, 26(11), 1091-1112.

[13] Messali, F. and Rots, J.G. (2017). Drift limits of URM rocking walls based on experimental in-plane tests. Delft University of Technology, version 10-03-2017.

Appendix A. Information on construction

In this Section information on the construction of the walls are provided.

In this experimental campaign three masonry type are use: CS brick and element masonry and solid clay brick masonry. Premixed mortar mixes are used in the construction. During the preparation of the mortar the following amount of water are used per bag of dry mix (25 kg): 2.8 L for CS brick masonry, 3.7L for solid clay brick masonry, 6 L for CS element masonry. A small concrete mixer is adopted for the preparation of the mortar. For each batch 2, 6 and 1 bags of dry mix mortar are mixed for the CS brick, clay and CS element masonry respectively.

The wall is supported in a steel frame composed by a bottom and top beam. The first and last courses of masonry are glued on the beams with Sikadur-30 epoxy. In the case of the CS element masonry, a first kicker layer is adopted composed by small masonry units (Figure 43).

Table 19 shows the dimensions of the walls after construction. The drawings of each wall are reported in Figure 48 to Figure 53.

(a) (b)

Figure 43 – (a) Gluing of first course of masonry; (b) Small units used for the kicker layer in CS element masonry walls.

Table 19 – As built dimensions.

	TUD_COMP-21	TUD_COMP-22	TUD_COMP-23	TUD_COMP-24	TUD_COMP-25
Height (mm)	L: 2700 M: 2694 R: 2690	L: 2695 M: 2697 R: 2695	L: 2699 M: 2699 R: 2704	L: 2715 R: 2715	L: 2715 R: 2715
Length ()	T: 2690 M: 2694 B: 2700	T: 3005 M:3000 B: 2995	T: 3005 M: 3000 B: 2995	T: 980 B: 979	T: 980 B: 977
Thickness (mm)	100	210	210	100	100
L= left, M = mid R= right, T=top, B=bottom					

The wall TUD_COMP-23 has a window opening with a masonry lintel. The lintel is a jack arch which is single wythe. On the back side of the lintel a wooden beam of 1200x100x50mm is place which covers the length of the window opening (Figure 44). The masonry on the back side of the jack arch continues over the wooden beam as in a single wythe running bond pattern.
A cutting template is used to cut the bricks of the jack arch into the correct shape for the jack arch (Figure 45). Cutting was done with a saw in combination with water. The bricks are dried for a few days before used for construction. Figure 46 shows the complete pre-cut jack arch and Figure 47 show the installation of the lintel.

Figure 44 - Wooden beam to support masonry above window opening

Figure 45 – Cutting template for jack arch

Figure 46 – Pre-cut jack arch

(a)

(b)

(c)

Figure 47 – Placement of pre-cut jack arch above window

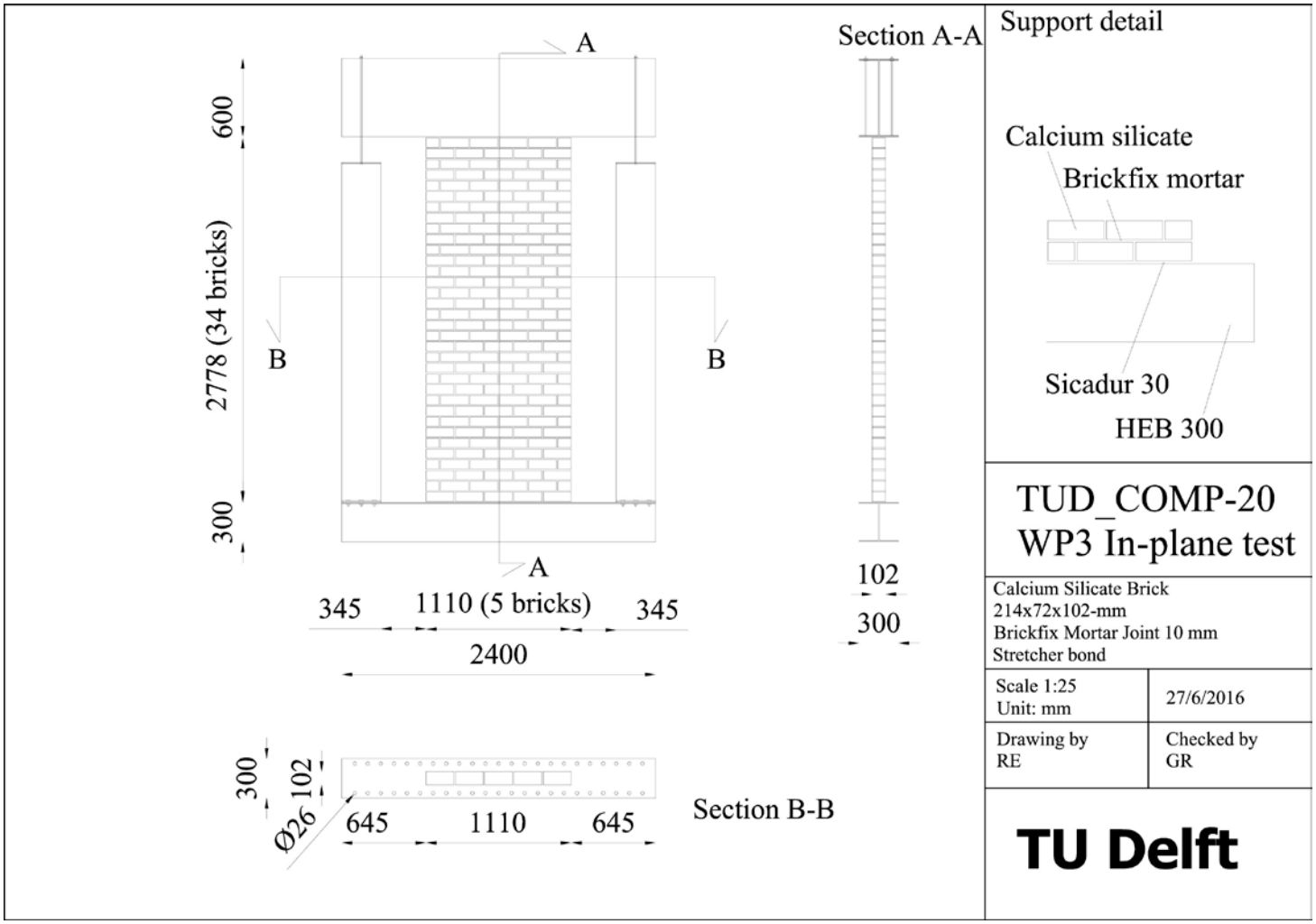

Figure 48 – Drawing adopted for the construction of wall TUD_COMP-20. As built dimension in Table 19.

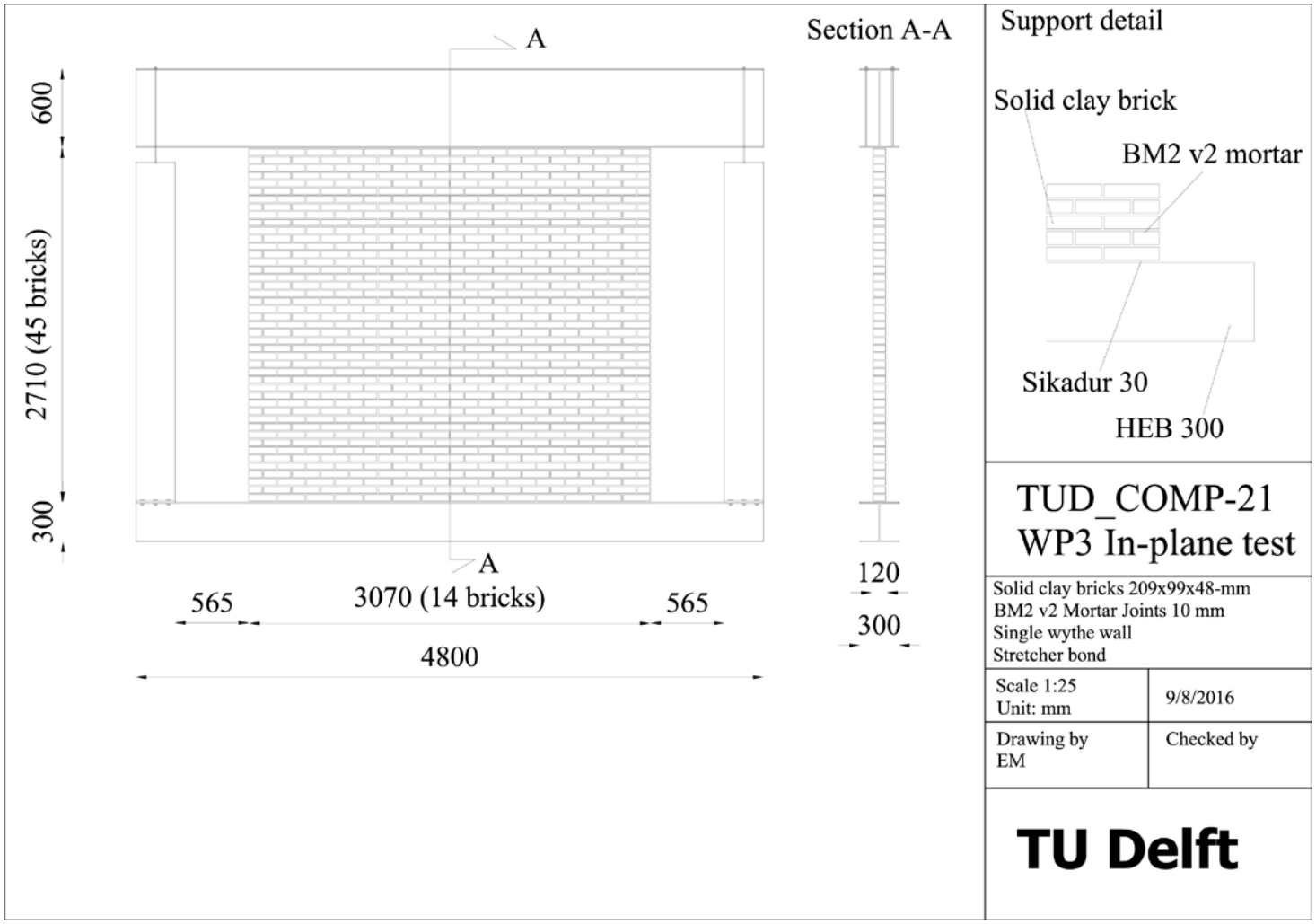

Figure 49 – Drawing adopted for the construction of wall TUD_COMP-21. As built dimension in Table 19.

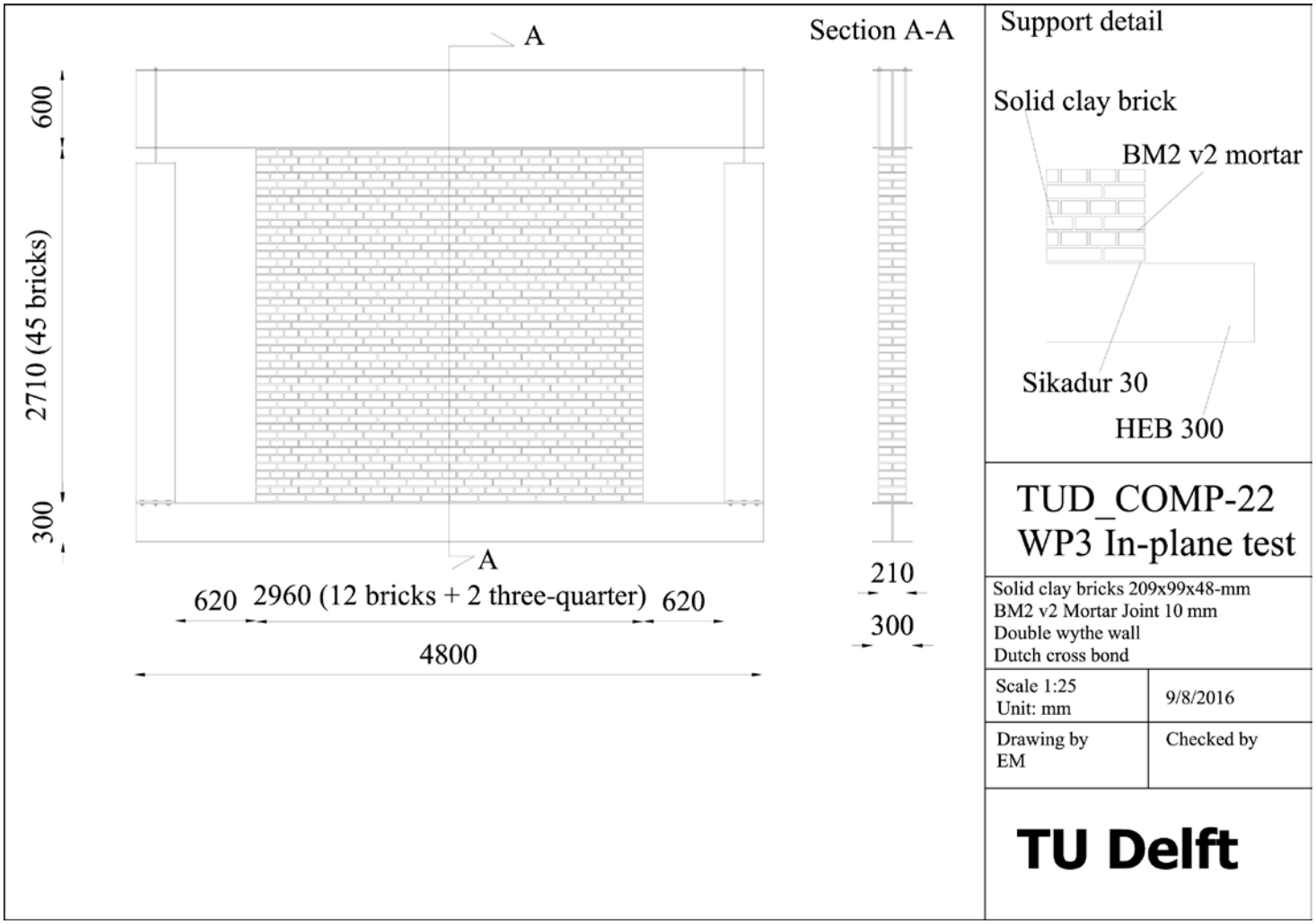

Figure 50 – Drawing adopted for the construction of wall TUD_COMP-22. As built dimension in Table 19.

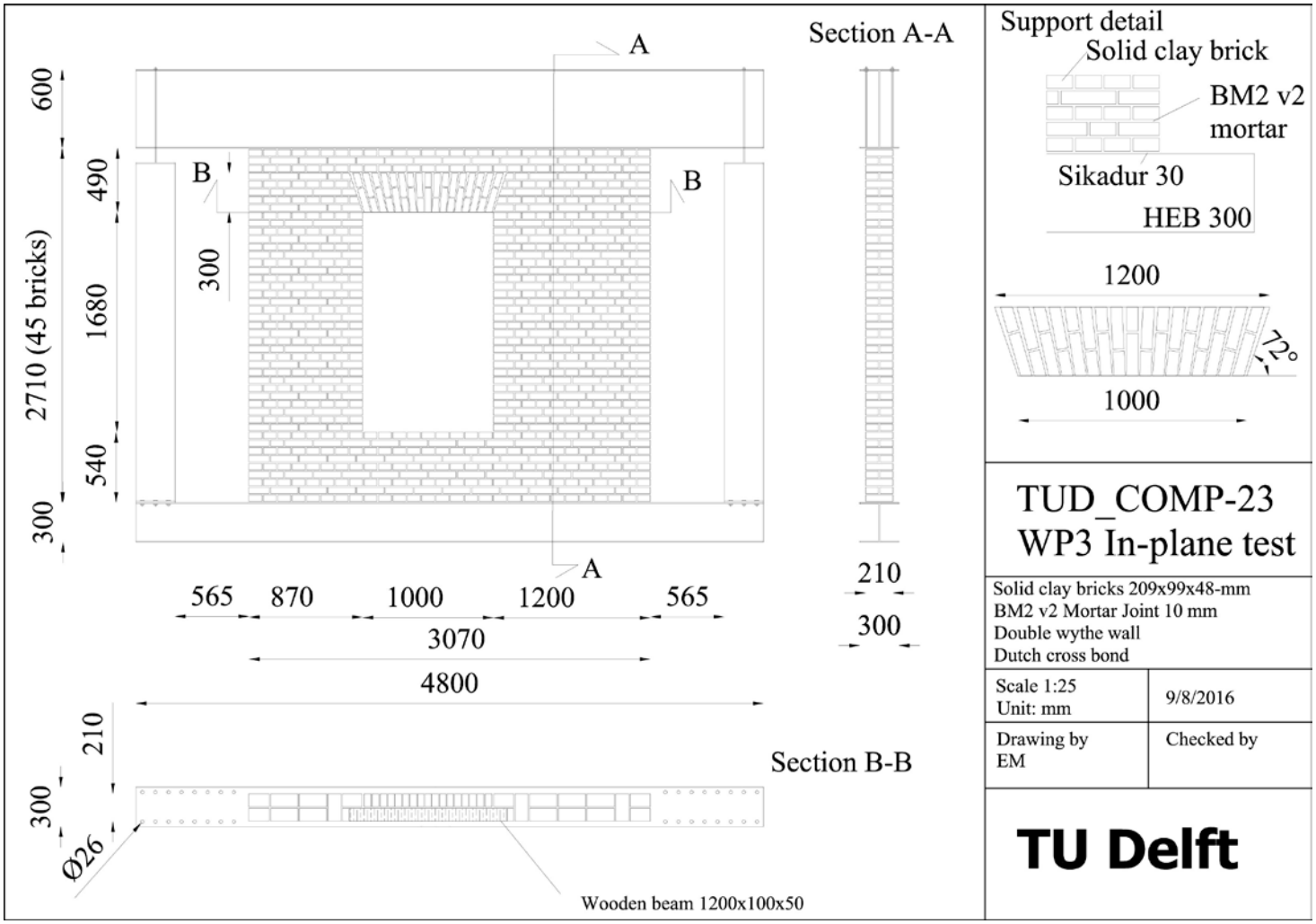

Figure 51 – Drawing adopted for the construction of wall TUD_COMP-23. As built dimension in Table 19.

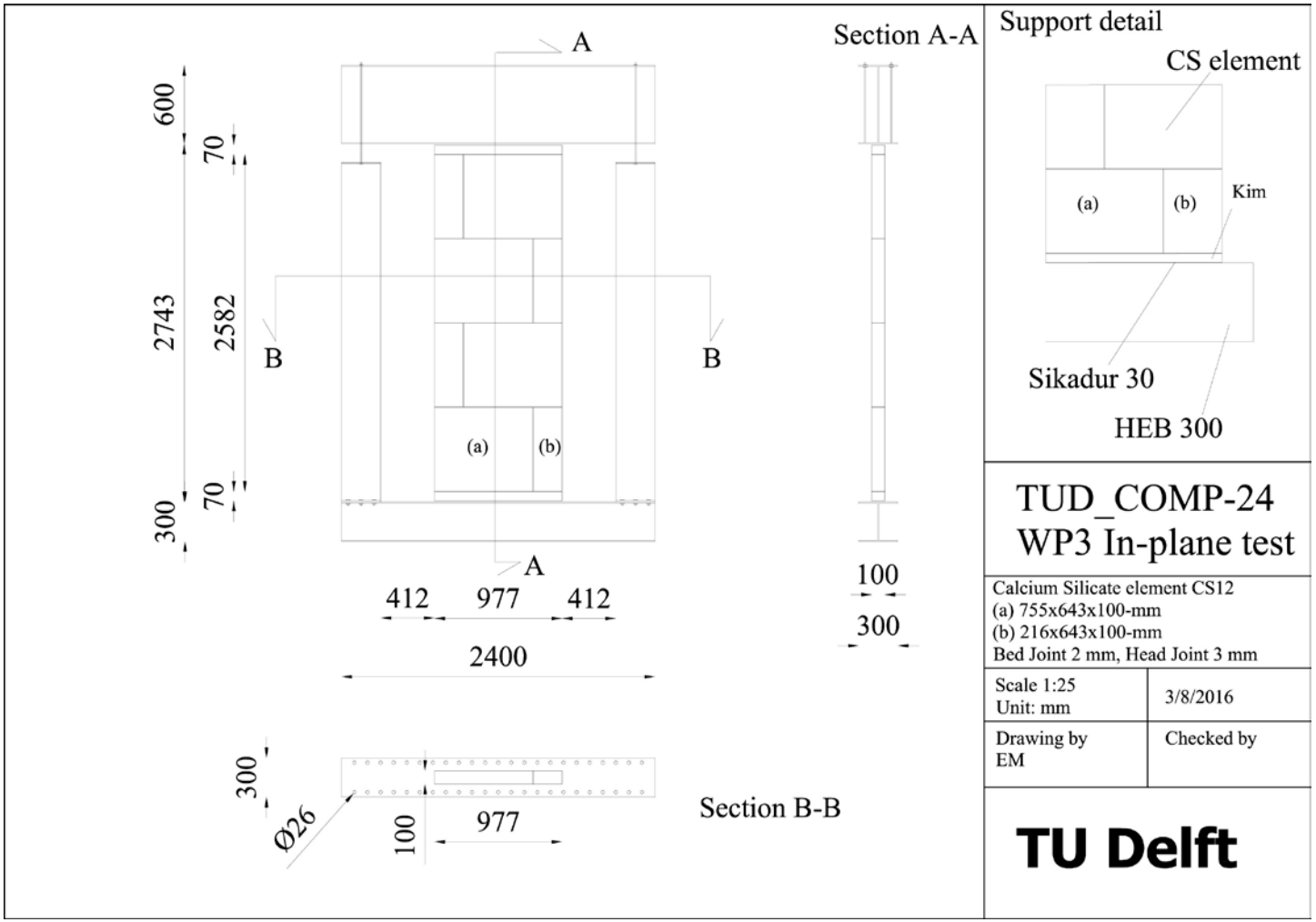

Figure 52 – Drawing adopted for the construction of wall TUD_COMP-24. As built dimension in Table 19.

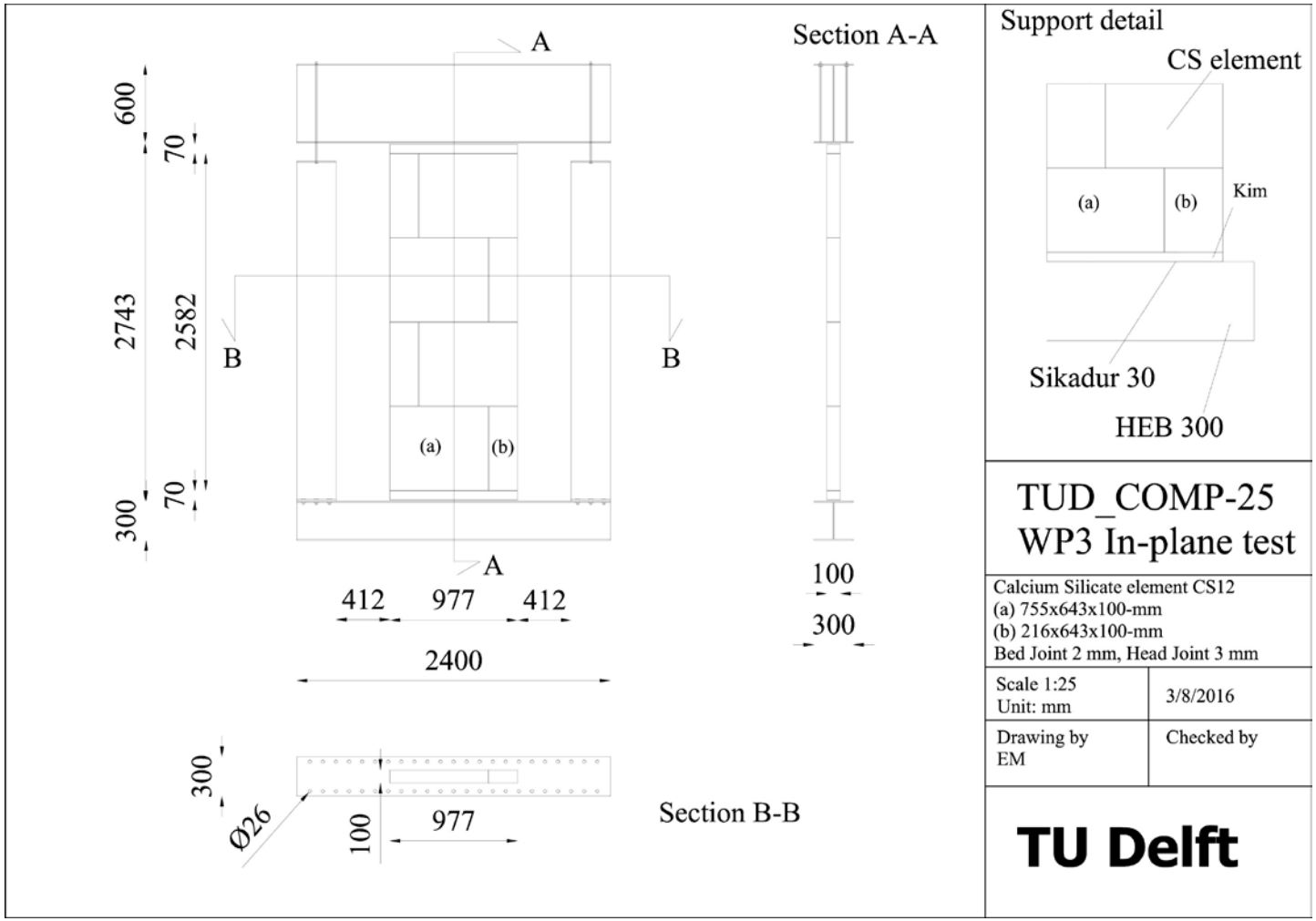

Figure 53 – Drawing adopted for the construction of wall TUD_COMP-25. As built dimension in Table 19.